TKK Reports in Forest Products Technology, Series A8
Espoo 2009

NOVEL METHODS TO CHARACTERIZE INK - COATING INTERACTIONS, COATING STRUCTURE AND SURFACE ENERGY

Doctoral thesis

Deqiang Ma

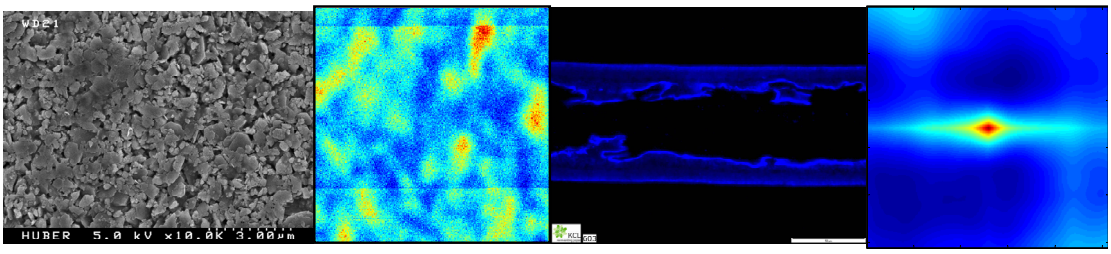

TEKNILLINEN KORKEAKOULU
TEKNISKA HÖGSKOLAN
HELSINKI UNIVERSITY OF TECHNOLOGY
TECHNISCHE UNIVERSITÄT HELSINKI
UNIVERSITE DE TECHNOLOGIE D'HELSINKI

TKK Reports in Forest Products Technology, Series A8
Espoo 2009

NOVEL METHODS TO CHARACTERIZE INK / COATING INTERACTIONS, COATING STRUCTURE AND SURFACE ENERGY

Doctoral thesis

Deqiang Ma

Dissertation for the degree of Doctor of Science in Technology to be presented with due permission of the Faculty of Chemistry and Materials Sciences for public examination and debate in Auditorium Puu II at Helsinki University of Technology (Espoo, Finland) on the 29th of May, 2009, at 12 noon.

TEKNILLINEN KORKEAKOULU
TEKNISKA HÖGSKOLAN
HELSINKI UNIVERSITY OF TECHNOLOGY
TECHNISCHE UNIVERSITÄT HELSINKI
UNIVERSITE DE TECHNOLOGIE D'HELSINKI

Distribution:
Helsinki University of Technology
Faculty of Chemistry and Materials Sciences
Department of Forest Products Technology
P.O. Box 6300
FIN-02015 TKK

ISBN 978-951-22-9881-5 (printed)
ISSN 1797-4496
ISBN 978-951-22-9882-2 (PDF)
ISSN 1797-5093
URL: http://lib.tkk.fi/Diss/2009/isbn9789512298822/

Picaset Oy
Helsinki 2009

ABSTRACT OF DOCTORAL DISSERTATION	HELSINKI UNIVERSITY OF TECHNOLOGY P.O. BOX 1000, FI-02015 TKK http://www.tkk.fi

Author Deqiang Ma

Name of the dissertation
Novel Methods to Characterize Ink/Coating Interactions, Coating Structure and Surface Energy

Manuscript submitted February 22, 2009	Manuscript revised April 23, 2009

Date of the defence May 29, 2009

☐ Monograph	x Article dissertation (summary + original articles)

Faculty Chemistry and Materials Sciences
Department Forest Products Technology
Field of research Forest Products Chemistry
Opponent(s) Prof. Lars Järnström
Supervisor Prof. Janne Laine
Instructor Prof. em. Per Stenius

Abstract

The main focus of this thesis is to analyze capillary adsorption of heterogeneous porous paper coatings. The approach is to develop a novel Gibbs energy model, analyze the structure and surface energy parameters of pilot coated paper and board samples, and compare results to ink tack kinetics.

Recent studies have modeled and verified that when inertial force and kinetic energy are included, a smaller diameter capillary starts to fill faster. In addition, other retarding forces, such as local transient sticking of the ink vehicle at surface asperities or chemical inhomogeneities, capillary surface topography and connections between capillaries or physical inhomogeneities in coating, affect the total rate of imbibition. While these resistant factors are very important none of them changes the fact that the basic force driving spontaneous imbibition is the total liquid sorption energy in all various capillaries.

This thesis suggests that the change in Gibbs free energy of a liquid associated with its imbibition into capillaries of coating can be used to describe such driving energy. It first derives an expression for this quantity then shows how specific Gibbs energy correlates with the time to reach maximum ink tack, tmax for carbonate-kaolin and latex based coatings. The application of the Gibbs energy model shows that for a relatively constant liquid-solid-vapor interface a larger capillary pore surface area strongly increases the rate of ink setting, as measured by the reduced tmax. In contrast, there is no correlation between ink tack development and pigment surface area or peak pore size of the coating which are currently in use. This new model analyzing Gibbs energy has advantages of combining porous structure variables (volume and diameter, $\Sigma(Vi/Di)$) and surface energy parameters ($\gamma\cos\theta$) at the interface which often vary concurrently when coating components change, and being independent of many details of time-dependent variables.

Surface topography affects liquid-solid-vapor/air interfaces. The second part of the thesis describes simultaneous characterization of surface topographies, using Near-field scanning optical microscopy. Finally, the thesis relates light scattering and absorption to the influence of fine kaolin and carbonates on coating structure and water soluble chemical such as fluorescence whitening agent distribution and efficiency in paper coating.

Keywords Coating structure, Gibbs energy, surface energy, capillary adsorption, topography, scattering

ISBN (printed) 978-951-22-9881-5	ISSN (printed) 1797-4496
ISBN (pdf) 978-951-22-9882-2	ISSN (pdf) 1797-5093
Language English	Number of pages 75 p. + app. 67 p.

Publisher Helsinki University of Technology, Department of Forest Products Technology

Print distribution Helsinki University of Technology, Department of Forest Products Technology

x The dissertation can be read at http://lib.tkk.fi/Diss/

PREFACE

This study was not possible without the generous encouragement and excellent guidance from Prof. Janne Laine. For years, Professor (emeritus) Per Stenius has given me his insight and broad knowledge on surface chemistry that built the foundation to the Gibbs free energy model development for capillary imbibition phenomenon. This study, which features a fundamental approach with direct industrial applications, could not bear fruits without the strong support from my boss, Dr. Douglas Carter at KaMin LLC. I am deeply indebt to each of them.

In addition to the Gibbs energy of thermal dynamic fundamentals at liquid-solid-vapor interface, this thesis also ventured efforts on light-solid-air interface in optic coating. It was Prof. Aristide Dogariu who guided me on optics that opened a colorful laser world in front of me, and helped me to introduce NSOM into smooth paper coatings. Because blade coating runs at 80-100 km/h, fluid dynamics has enormous influence over liquid-particle-blade interactions, influencing 3D coating structure formation. Prof. Douglas Bousfield coached me on computer simulations of coating color flow in a shear field. Prof. Martti Toivakka is thanked for his great teaching on my minor study. I feel extremely fortunate and grateful for having their great guidance.

I also want to thank:

* Dr. Susanna Holappa at the Department of Forest Products Technology of Helsinki University of Technology for arranging lab measurements.

* PhD candidate David Haefner at the College of Optics and Photonics of Central Florida University for his diligent measurements of NSOM, and as the co-author of two papers.

* PhD candidate Jong Sonn at the Department of Chemical and Biological Engineering of University of Maine for teaching me running micro-tack device and continuing the measurements.

* My co-workers Brent Nobles, Aubrey Smith, John Taylor, and Tracy White for helping me on pigment and coating characterizations.

* Mrs. Ritva Vuorinen for working on the abstract format.

* PhD candidate Jani Salmi for helping with the thesis format and for ensuring that our “printing jobs” are correct and on time.

* My friends in Finland and America for their ongoing support and friendship

It has been my honor and pleasure to know and work with all of them!

Lastly, my wife, Jingwei and son, Jun (Jimmy) have been firmly beside me throughout this process. Jingwei has sacrificed her personal time and devoted her energy in supporting me 24x7. Jimmy didn’t ask much of my time and graduated from Emory University among top 100 out of 1600 undergraduates. We are very proud parents! It is their unconditional love that keeps me going!

Warner Robins, Georgia, USA, April 30th, 2009

Deqiang (Dan) Ma

LIST OF PUBLICATIONS

This thesis is based on the results presented in seven publications which are referred to by Roman numbers in the text. Papers I-III focus on developing a novel model of using Gibbs free energy to describe capillary adsorption. Paper IV uses Near-field scanning optical microscopy (NSOM) to simultaneously characterize coated paper surface topography and optical contrast. Paper V investigates the whole coating structure influence on water soluble fluorescence whitening agent distribution and efficiency in coatings. Paper VI and VII give practical and computer simulation results of coating structures.

Paper I

Ma, D., Carter, R. D., Laine, J. and Stenius, P. (2007): Gibbs energy analysis of ink oil imbibition during ink setting*, Nordic Pulp and Paper Research Journal,* 22(4), 523-527.

Paper II

Ma, D., Carter, R. D., Laine, J. and Stenius, P. (2008a): Gibbs energy of imbibition of non-polar and polar solutions into calcium carbonate and kaolin coatings, *Nordic Pulp and Paper Research Journal,* 23(3), 333-337.

Paper III

Ma, D., Carter, R. D., Laine, J. and Stenius, P. (2009): The influence of coating structure and surface energy on Gibbs energy of ink oil imbibition during ink setting, *Nordic Pulp and Paper Research Journal,* 24(2), to be published in June, 2009.

Paper IV

Ma, D., Carter, R.D, Haefner, D. and Dogariu, A. (2008b): Simultaneous characterization of coated paper topography and optical contrast by Near-field scanning optical microscopy (NSOM), *Nordic Pulp and Paper Research Journal,* 23(4), 438-443

Paper V

Ma, D., Carter, R.D, Haefner, D. and Dogariu, A. (2008c): The influence of fine kaolin and ground calcium carbonates on the efficiency and distribution of fluorescence whitening agents (FWA) in paper coating, *Nordic Pulp and Paper Research Journal,*23(3), 327-332.

Papers presented at Conferences

Paper VI

Ma, D., Carter, R.D, Chen, C. and Hardy, R.H. (2005): Print mottle reduction through clay engineering and pore structuring in paper coating, TAPPI Proc. Coating Conf. Toronto, April 17-20, 2005, TAPPI Press, CD-Rom, Session 27.

Paper VII

Ma, D., Carter, R.D, and Bousfield, D. W. (2008): Prediction of coating structure change during calendering, 10th TAPPI Coating Fundamental Symposium, Montreal, June 11-13, 2008, TAPPI Press, Atlanta, pp121-132.

Author's contribution to the appended joint publications:

In Papers I-III, Deqiang Ma developed a novel model of charaterizing ink and coating interactions using Gibbs free energy concept with inclusions of heterogeneous porous medium structure and liquid-solid-vapor interface in capillary adsorption. He also designed and performed coating experiments, measured contact angles, coating pore size and volume distributions, calculated Gibbs energy and wrote the manuscipts. In Paper IV and V, Deqiang Ma proposed the basic approaches following surface chemistry and optics fundamentals, designed and performed the coating experiments, analyzed the results, and wrote the manuscripts while College of Optics and Photonics of Central Florida University, USA and Finnish Pulp and Paper Research Institute deligently performed measurements of NSOM and optical microscopy under UV light, respectively. In Paper VI and VII, Deqiang Ma designed coating and calendering, and simulated the particle rotation in a shear field with the software developed by Univeristy of Maine, USA. The co-authors of publications contributed to theoretical discusssions.

LIST OF SYMBOLS

AFM	Atomic force microscopy (sec. 7.3)
$C(N, \Delta\theta)$	Optical contrast (sec. 7.2)
$C(r)$	Autocorrelation function (sec. 7.1)
D_i	Diameter filled with liquid (sec. 3.3)
DIM	Diodomethane (sec. 4.3)
DOE	Design of experiment (sec. 10.1)
EDS	Energy dispersive spectrometry (sec. 5.5)
EO	2-ethoxyethanol (sec. 4.3)
F_{max}	The maximum ink tack force (sec. 5.6)
FMD	Formamide (sec. 4.3)
FWA	Fluorescence whitening agents (sec. 10)
ΔG_L	Gibbs energy of an incompressible liquid (sec. 3.3)
ΔG_s	Specific Gibbs energy (sec. 3.3)
$H(r)$	Height-height correlation function (sec. 7.1)
h_i	The length of the cylinder filled with liquid (sec. 3.3)
$\boldsymbol{I_i}$	Irradiance (sec. 10.1)
N	The number of “equivalent scattering centers” (sec. 7.2)

NSOM	Near field scanning optical microscopy (sec. 7.3)
ΔP	The pressure drop across a curved interface (sec. 3.3)
R	Reflection coefficient (sec. 10)
rms	Root mean square (sec. 7.1)
SEM	Scanning electron microscopy (sec. 8.1)
t_{max}	Time needed to reach the maximum ink tack force (sec. 5.6)
T_{slab}	Transmittance through the slab (sec. 10)
V_i	Liquid volume in the *i*th capillary (sec. 3.3)
$\sum(V_i/D_i)$	Coating structure variables (sec. 5.7)
w	Interface width (sec. 7.1)
α_{abs}	Light absorption coefficient (sec. 10)
α_{EXT}	Light extinction coefficient (sec. 10)
α_{scatt}	Light scattering coefficient (sec. 10)
γ	Liquid surface tension (sec. 3.4)
γ^{AB}	Short-range Lewis acid-base interactions (sec. 3.5)
$\gamma cos\theta$	Surface energy parameters (sec. 5.7)
γ^{d}	The contribution of dispersion (London) interactions (sec. 3.4)

γ^{LW}	Lifshitz-van der Waals interactions, includes London (dispersion), Keesom (dipole-dipole) and Debye (dipole-induced dipole) interactions (sec. 3.5)
γ^{p}	Includes all other interactions, collectively called "polar" interactions (sec. 3.4)
γ^{+}	Acid component (sec. 3.5)
γ^{-}	Basic component (sec. 3.5)
λ	Wave length (sec. 10)
μ	Fluid viscosity (sec. 3.3)
$\Delta\theta$	The phase distribution of scattering centers (sec. 7.2)
ρ_v	Volume density of pores (sec. 10)
σ_s	Scattering cross-section (sec. 10)

TABLE OF CONTENTS

1. INTRODUCTION AND OUTLINE OF THE STUDY

The work was started and mainly conducted at Huber Engineered Materials, Macon, Georgia (now KaMin LLC), USA and the Department of Forest Products Technology of Helsinki University of Technology, Espoo, Finland. A part of the research work focusing on coated paper surface topography and optical contrast characterizations was completed in cooperation with the College of Optics and Photonics of Central Florida University, Orlando, Florida, USA. Computer simulation work of particle flows was done by using software developed by University of Maine, USA.

The overall aim of this study is to analyze capillary adsorption in heterogeneous porous coating by applying thermodynamic fundamentals on a macro scale. The main focus is to take a novel fundamental approach using Gibbs energy concept to investigate capillary adsorption in coatings. The objective of the second part is to simultaneously characterize the surface topography that affects wetting phenomena and optical contrast, applying Near-field scanning optical microscopy to paper coating research. The optical near field features light wave length distance, and therefore has great potential in thin layer coating with nano particles on a micro scale. The objective of the third part is to study the influence of fine kaolin and calcium carbonates on coating structure and, in turn, its impact on water soluble chemical such as fluorescence whitening agent distribution and efficiency.

PART A (Papers I-III) presents a Gibbs energy analysis of ink oil imbibition during ink setting. The specific change in Gibbs energy, ΔG_s, when a probe liquid is imbibed in a porous medium, is calculated from the capillary diameter and volume of the pores, and the surface tension and contact angle of the liquid. Capillary pore volumes and equivalent pore diameters of a series of double coated and super calendered paper samples are determined by mercury porosimetry. ΔG_s of imbibition of diiodomethane (DIM), water, and binary solutions of formamide (FMD), water and 2-ethoxyethanol (EO) with surface tensions 40, 50, 60 and 70 mJ m^{-2} into six coatings are calculated. Dispersive and polar components of surface energies of coatings are evaluated from contact angles of water and DIM, using the Owens and Wendt approach. The time to reach the maximum tack force, t_{max} of an oil-based offset ink is measured for all coatings. The relative chemical concentrations are investigated by energy dispersive spectroscopy (EDS).

In paper coating experiments, the studies describe pigment types *i.e.* calcium carbonate and kaolin (aluminosilicate) influence on ΔG_s when different polarity liquids are used (Papers I-II). The studies show that ΔG_s associated with imbibition of probe liquid into porous coating can basically be treated as a product of coating structure variables (volume and diameter, $\sum(V_i/D_i)$) and surface energy parameters ($\gamma cos\theta$, in which γ is the liquid surface tension and θ is the contact angle at the interface), *i.e.* ΔG_s highlights interactive properties of the porous coating surface and probe liquid. In board coatings where higher level of kaolin and latex are used, it presents their chemistry influence on ΔG_s (Paper III). The investigation shows that ΔG_s with coating structure variables (volume and diameter, $\sum(V_i/D_i)$) and surface energy parameters ($\gamma cos\theta$) are affected by changes in kaolin and latex chemistries. It demonstrates that compared to styrene/n-butyl acrylate latex, n-butyl acrylate-acrylonitrile-styrene latex lowered γ^{LW} on coated board surface, and significantly increased t_{max}, and reduced the maximum tack force, F_{max}, and the final tack.

PART B (Paper IV) introduces a simultaneous characterization of coating topography and optical contrast by Near-field scanning optical microscope (NSOM), with verifications by scanning electron microscope (SEM) and atomic force microscope (AFM). This study demonstrates that the NSOM provides a unique capability of measuring simultaneously the information about both local topography and optical contrast at resolutions better than conventional far-field techniques. This study shows that the addition of fine kaolin increases the topography correlation length resulting in a smoother varying surface contour. Furthermore, the topography correlation length increases with different amounts in orthogonal directions indicating the creation of a certain degree of surface anisotropy.

PART C (Paper V) characterizes fluorescence whitening agents (FWA) efficiency by TAPPI brightness and ISO CIE whiteness. Classic optical theory applications in light transmittance are further verified by another pilot scale coating with mixture design of experiment (DOE). FWA distribution is studied by optical microscopy of coated paper cross section under UV light. This study demonstrates that increasing fine kaolin level at the expense of narrow GCC makes FWA concentrate more towards the surface. Based on optical calculations and experiment results, it proposes desired coating structure and FWA distribution for high UV light efficiency in coatings.

2. PART A, BACKGROUND AND MODEL DEVELOPEMENT

2.1 The need to analyze capillary adsorption using Gibbs energy

In general, pigment coating is considered as surface treatment for improving paper and board surface and structure properties. The coated surface often provides a smooth texture with good optical and topography for printing. Depending on coating ingredients used, a thin coating layer featuring a few to tens micrometers can have very different physical and chemical surface and structure properties. Such a layer physically and chemically interacts with oil and aqueous liquids contained in printing and packaging, hence it is important to study the coating physical structure and chemical property together.

The critical parameters of coating structure having an influence on liquid imbibition on ink setting, film split and leveling are the nature of the liquid-solid-vapor interface as well as the capillary diameter and pore volume distributions. Capillaries of a given volume with small diameters tend to have a relatively stronger influence on the ink tack build rate than capillaries with a larger diameter but a marginally larger pore volume (Paper VI). It was therefore felt that some way of characterizing the pore structure and surface energy that correlates better with ink tack than pore diameter or volume distribution alone was needed. This part suggests that the change in specific Gibbs energy of a liquid associated with its imbibition into the capillary of a porous medium may provide such characteristics. It first derives an expression for such a quantity then proceeds to show how specific Gibbs energy correlates with the time to reach the maximum ink tack for some carbonate-kaolin and latex based paper coatings featuring a heterogeneous porous medium.

2.2 Imbibition of ink vehicle into porous coatings

A simple model of the kinetic imbibition into a capillary is the well-known Lucas-Washburn (LW) equation (Washburn, 1921). This equation was derived from the assumptions that the driving forces (capillary pressure and external pressure) are balanced by frictional forces in the liquid, that the movement of the liquid-solid-vapor contact line is unimpeded (*i.e.* the capillary wall is smooth and homogeneous), that the reservoir of liquid is infinite and that the flow is described by the Poiseuille equation for laminar flow.

For the flow in a single straight capillary, the LW equation has been successfully used in interpretations of results from basic studies of systems with simple shape (e.g. Levine et al. 1976; Fisher, Lark 1979), and extended to water and cyclohexane in glass capillaries ranging from 0.3 to 400 μm in radii (Rye et al. 1996). The LW is valid for large times where all influences other than capillary and friction forces are negligible (Jeje 1979; Joos et al. 1990). Recent studies have modeled and verified that when inertial force and kinetic energy are included, a smaller diameter capillary starts to fill faster than a larger one; the rate is proportional to t^2 (time) in initial stage, proportional to t during short transition period, then very soon dependent linearly on $t^{(1/2)}$ and capillary diameter as predicted by the LW (Stange et al. 2003). However, several industrial experimental studies have shown that a direct application of the LW equation for a flow in a single capillary to describe the vehicle removal from ink film into a heterogeneous porous coating is, at best, very limited (Donigian et al. 1996; Preston et al. 2002; Schoelkopf et al. 2003a; Xiang et al. 2004). Contrary to the prediction by the LW equation, the initial imbibition preferentially takes place into capillaries with very small diameters, due to the inertia force of the liquid (Bosanquet 1923). Furthermore, imbibition is slower than predicted, partly due to the thickening of the ink that is the source of the liquid (Schoelkopf et al. 2003a, 2003b), and the liquid wets and flows over a rough and heterogeneous solid surface. In addition, many liquid-solid-vapor interface phenomena are involved, such as surface forces, wetting thermodynamics and statistical physics of pinning of the contact line and wetting transitions (de Gennes 1988). For spreading liquids or liquids with very low contact angle on capillary wall, the actual meniscus may be preceded by a thin liquid film (Derjaguin et al. 1976, Beaglehole 1989), with a thickness varying from less than a nanometer to several nanometers. Liquid profiles in the vicinity of the contact line are consistent with either slip or thin film boundary conditions (Dussan 1991; Rame, Garoff 1996). Hence, the flow at the front edge of the liquid is very difficult to characterize (Marmur 1992). In addition, local wetting properties and pore geometry determine the curvature of the meniscus, resulting in variations in the local capillary pressure. Taken together, all these factors make direct application of the LW equation to ink vehicle removal due to capillary sorption difficult.

2.3 Gibbs free energy of liquids in a porous medium

A detailed understanding of the mechanism by which capillaries in a heterogeneous porous medium are spontaneously filled by liquid is of general interest, for example, in the material

development of coatings and catalysts, textile, oil recovery, and space technology. Models describing this process generally involve several parameters that are not easily accessible experimentally (Lavi et al. 2008). On the other hand for a routine characterization and comparison of ink imbibition and development of ink tack on different coatings one needs some basic characteristics that can be determined rapidly and with reasonable accuracy. For this purpose, the BET surface has been used as a measure of pigment specific surface area and mercury porosimetry has been utilized to calculate the distribution of capillary diameters and volumes. Interpretation of porosimetry is usually based on the simplifying assumption that all capillaries are more or less cylindrical. However, the correlation of such data with ink tack, which is an important phenomenological characteristic of ink setting on porous coating, often leaves much to be desired. This thesis will show that the change in specific Gibbs energy (ΔG_s) of the imbibed ink vehicle when it is subjected to the capillary pressure correlates in a better way with development of ink tack. ΔG_s is a general characteristic which is directly related to capillary size and volume distribution, and interface surface energy. This approach analyzing the sorption energy has an advantage of being independent of many details of time-dependent processes mentioned above and can be calculated in the following way.

The effect of a change in mechanical pressure at constant temperature on the molar Gibbs energy of an incompressible liquid (constant molar volume) is given by

$$\Delta G_L = \int_{P_0}^{P_0+\Delta P} V_L dP = V_L \Delta P \,, \qquad [2\text{-}1]$$

where V_L is the molar volume of the liquid and P is the pressure

The pressure drop, ΔP, across a curved interface is given by the Laplace equation

$$\Delta P = \gamma \left(\frac{1}{R_1} + \frac{1}{R_2} \right), \qquad [2\text{-}2]$$

where γ is the liquid-vapor surface tension and R_1 and R_2 are the two radii of the curvature (e.g., Adamson and Gast, 1997). We make a simplifying assumption that the capillaries are cylindrical with circular cross-section. Then, given that a liquid penetrating into a capillary forms an approximately spherical meniscus with a contact angle θ at the interface, $R_1 = R_2$

$=D/2\cos\theta$, where D is the diameter of the capillary, and θ is the contact angle of the liquid at the capillary wall. Thus *Eq. 3-3* can be written (Fisher and Israelachvili, 1981)

$$\Delta P = -\frac{4\gamma \cos\theta}{D}. \qquad [2\text{-}3]$$

Substitution into *Eq. [2-1]* gives

$$\Delta G_L = -V_L \frac{4\gamma \cos\theta}{D}, \qquad [2\text{-}4]$$

where the negative sign accounts for the fact that penetration will be spontaneous for a wetting liquid ($\cos\theta > 0$). *Eq. [2-4]* is valid throughout the whole capillary imbibition process at any given time and location. In the final state at equilibrium, for the imbibition of liquid into a distribution of independent cylindrical capillaries, the Gibbs energy of any capillary with diameter D_i that is filled with liquid of volume V_i is

$$\Delta G_i = -V_i \frac{4\gamma \cos\theta}{D_i}. \qquad [2\text{-}5]$$

For very small capillaries it may be necessary to take into considerations of the liquid volume in thin films formed on the capillary walls. However, for want of detailed knowledge about the surface forces and the fraction of capillaries that are small enough for the film volume to be of importance, we shall neglect the volume of any precursor films formed. Then

$$V_i = \frac{\pi D_i^2}{4} h_i, \qquad [2\text{-}6]$$

where h_i is the length of the cylinder filled with liquid. Substitution of *Eq. [2-6]* into *Eq. [2-5]* gives

$$\Delta G_i = -4A_i h_i \frac{\gamma \cos\theta}{D_i} = -\frac{\pi D_i^2 h_i}{4} \cdot \frac{4\gamma \cos\theta}{D_i} = -\pi D_i \gamma h_i \cos\theta, \qquad [2\text{-}7]$$

where A_i is the cross-sectional area of the capillary.

Several things may be noted about *Eq. [2-7]*. It is the work done by the surface tension that moves the liquid along the wall of a capillary to a length of h_i. At a given contact angle and surface tension the product of diameter and length determines the change in Gibbs energy when the liquid is imbibed. For the vertical rise of liquid in a capillary against gravity, h_i increases until the capillary force ($\pi D_i \gamma cos\theta$) equals to the total weight of the column of liquid (Adamson and Gast, 1997). *Eq. [2-7]* describes imbibition from an unlimited source of liquid. It may be extended to describe capillary desorption that usually balances the advancing capillary sorption when there is a locally insufficient supply of liquid such as in coating, painting and printing. However, caution has to be used in this case, since there is usually a sorption/desorption (or contact angle) hysteresis. Furthermore, $\pi D_i \gamma cos\theta$ in *Eq. [2-7]* is the exact form of capillary force in the expanded Bosanquet equation that describes the dynamic balance of forces in a capillary when gravity is neglected but the inertia of the penetrating liquid is taken into account (Ichikawa, Satoda 1994):

$$\gamma \cos\theta \cdot \pi D - 8\pi\mu \cdot h\frac{dh}{dt} = \rho\pi\frac{D^2}{4}\left\{(h+x)\frac{d^2h}{dt^2} + \frac{n}{2}\left(\frac{dh}{dt}\right)^2\right\}, \qquad [2\text{-}8]$$

where μ is the liquid viscosity, and ρ is liquid density; x and n are the correction factors for the inertial force and energy dissipation, respectively.

For a distribution of independent capillaries in a porous material, the total change in Gibbs energy ΔG_t can be calculated by summarizing over all capillaries:

$$\Delta G_t = \sum_i \Delta G_i = \sum_i -4A_i h_i \frac{\gamma cos\theta}{D_i} = \sum_i -\frac{4V_i \gamma cos\theta}{D_i}. \qquad [2\text{-}9]$$

Thus if the surface tension of the liquid and its contact angle at pore walls are known and the volume and size distributions of capillaries can be determined, the effect of the change in pressure on the Gibbs energy of the liquid when imbibed into a porous structure at constant temperature may be calculated. A "specific" Gibbs energy, ΔG_s can be calculated as the change in Gibbs energy per mass of dry porous material, m:

$$\Delta G_s = \sum_i \frac{\Delta G_i}{m} = \sum_i \Delta G_{s,i}. \qquad [2\text{-}10]$$

2.4 Surface energy theories

2.4.1 Polar and non-polar components

In the Good-Girifalco-Fowkes approach (Girifalco, Good 1957; Fowkes 1962) for the interpretation of surface tensions and adhesion, the contribution of different interactions to the surface tension γ is divided into two groups

$$\gamma = \gamma^d + \gamma^p, \qquad [2\text{-}11]$$

where γ^d is the contribution of dispersion (London) interactions, often also denoted "non-polar" interactions and γ^p includes all other interactions, collectively called "polar" interactions. In paper coating study, the main interest was in the comparison between coatings containing different amounts of similar components *i.e.* calcium carbonates, aluminosilicates, and therefore a fist step was to use the simple approach Owens and Wendt to interpret polar interactions (Owens, Wendt 1969), *i.e.*

$$\gamma_{SL} = \gamma_S + \gamma_L - 2\sqrt{\gamma_S^d \gamma_L^d} - 2\sqrt{\gamma_S^p \gamma_L^p}, \qquad [2\text{-}12]$$

in combination with Young's equation, which is valid for a liquid on a smooth, non-deformable and non-absorbing solid surface,

$$\gamma_S = \gamma_{SL} + \gamma_L \cos\theta, \qquad [2\text{-}13]$$

to give the equation

$$(1+\cos\theta)\gamma_L = 2\left(\sqrt{\gamma_S^d \gamma_L^d} + \sqrt{\gamma_S^p \gamma_L^p}\right). \qquad [2\text{-}14]$$

By measuring the contact angles of two liquids (usually one polar and one non-polar) with known values of γ_L, γ_L^d and γ_L^p the values of γ_S^d and γ_S^p can be determined.

2.4.2 Lifshitz-van der Waals and Lewis acid-base components

The Owens and Wendt approach is limited to non-polar and polar components. van Oss et al. (1988) suggested that surface energy γ be divided into two groups:

$$\gamma = \gamma^{LW} + \gamma^{AB}, \qquad [2\text{-}15]$$

where the first term, Lifshitz-van der Waals interactions, includes London (dispersion), Keesom (dipole-dipole) and Debye (dipole-induced dipole) interactions, and the second term denotes more short-range Lewis acid-base interactions. To take into account that material surfaces may contain both acidic and basic groups, the γ^{AB} term in *Eq. [2-15]* has been further divided into acid and base parameters (van Oss 2006)

$$\gamma^{AB} = 2\sqrt{\gamma^{+}\gamma^{-}}, \qquad [2\text{-}16]$$

where $\gamma^{+}$and γ^{-} denote acid and base parameters, respectively. In this approach (the van Oss-Chaudhury-Good, vOCG, approach), surface energy components can be determined by measuring contact angles for three liquids with known *LW*, $\gamma^{+}$and γ^{-}, and solving for the components, using the equation

$$(1+\cos\theta)\gamma_L = 2\left(\sqrt{\gamma_S^{LW}\gamma_L^{LW}} + \sqrt{\gamma_S^{+}\gamma_L^{-}} + \sqrt{\gamma_S^{-}\gamma_L^{+}}\right). \qquad [2\text{-}17]$$

The vOCG approach was used in the coated board study to evaluate the *LW* and *AB* components for kaolin and latex chemistry influence on surface energy.

3. PART A, EXPERIMENTAL

3.1 Materials

3.1.1 Pigments and paper coatings

For paper coating, ground calcium carbonates (GCC) with broad size distribution (broad GCC) and with narrow size distribution (narrow GCC) were from Omya AG. Precipitated calcium carbonate (PCC) with narrow size distribution (narrow PCC) was from Specialty Minerals. The fine kaolin was from Huber Engineered Materials. Particle size distributions of pigments were determined by sedimentation analysis (Sedigraph) and the specific surface area was determined by BET analysis (nitrogen) at laboratories of KaMin LLC, Macon, Georgia, USA (*Table 3-1*).

Table 3-1 Particle size distribution and BET area of the pigments. Broad = broad particle size distribution; Narrow = narrow particle size distribution (Paper I and II).

Pigment	**BET area**	**Cumulative particle size distribution**				
	m^2/g	< 5 µm %	< 2 µm %	< 1 µm %	< 0.5 µm %	< 0.2 µm %
Broad GCC	12.6	99.6	94.1	70.6	42	20.3
Narrow GCC	14.5	99.9	98.4	86.8	51.9	19.6
PCC	14.2	99.8	98.6	93.9	69.9	17.9
Fine Kaolin	21.2	99.1	97.2	93.7	79.7	44.1

A selection of coatings with different combinations of pigments, designed to represent a range of coating compositions with variable porosities, were prepared. The selection is typical of the current major top coating pigments of double-coated fine paper. The recipes used but not limited to (a complete formulation is listed in *Table 4-4a*) are given in *Table 3-2*. The coatings were prepared on a pilot scale according to the pilot coating facility procedures as following.

Table 3-2 Pigment compositions of coatings, in parts by weight. In addition, all coatings contained 0.15 parts PAA (Ciba Chemicals), 12 parts latex (Dow Chemicals) 0.5 parts CMC (CpKelco), 0.7 parts OBA (Bayer), 0.7 parts lubricant (Devden) and 0.3 parts cross linker (Bercen) in Paper I.

Topcoat	**A**	**B**	**C**	**D**	**E**	**F**
Fine kaolin	20	40	20	40	20	40
Broad GCC	80	60				
Narrow GCC			80	60		
PCC					80	60

The coatings were applied on woodfree base paper using a pilot coater at the Centre International de Couchage, Trois-Rivières, PQ, Canada. The pilot coater was run at 1400 m/min. The Opti-Concept™ Jet applicator + blade coating stations from Metso Paper were used. Moisture and coat weigh profiles were on-line measured with infrared and X-ray analysis but open-loop controlled, *i.e.* with operators' intervention. The base paper was precoated with 100% coarse ground calcium carbonate with 12 parts of latex, and chemical additives. The coat weight was 12 g/m^2 and run at 66% solids. Precoat formulations and process were kept constant for all the six coating trial points. Top coating solids targets were 65% with no on-line dilution. Drying automation was used to control the zone of first immobilization point and machine-direction temperature profile. An accurate control of top coat weight of ~ 5000 *m* long paper coating is essential for a random sample selection of reproducible capillary volume calculations from mercury porosimetry. The low surface roughness reduces the hysteresis of contact angle measurements. Coating pilot parameters are given in *Table 3-3*. Details are listed elsewhere (Papers I-II).

Table 3-3 Coating pilot parameters

Speed	Drying	Precoat weight, g m^{-2}	Topcoat weight, g m^{-2}	Topcoat Stdev, g m^{-2}	PPS-10* μm
1400 m/min	IR + Hot air	12	12	0.2-0.4	0.6-0.7

*) PPS-10 surface roughness, determined according to TAPPI Standard T555.

3.1.2 Latex and board coatings

For board coating, GCC was from Omya AG, and two types of fine kaolin of different processes were from KaMin LLC (*Table 3-4*). The ratio of kaolin to GCC was fixed to 50/50 for all four conditions. Styrene-acrylate based latexes (*x* and *y*) were from BASF AG. Latex *x*

was styrene/n-butyl acrylate copolymer with glass transition point of 23 °C at pH 6.5-7.5. Latex *y* was n-butyl acrylate-acrylonitrile-styrene copolymer with glass transition point of 4 °C at pH 7-8, according to the manufacturer. Coatings were applied, using the same pilot coater as for paper coating, on solid bleached sulfate board pre-coated at 400 m/min and 12 g/m^2 of 100 parts coarse GCC with 15 parts of latex, as well as optical brightener, thickener, dispersant, lubricant and cross-linker, the same chemicals as in top coat.

Table 3-4 Ground calcium carbonate and kaolin particle size distributions (PSD) and specific surface area (BET). The two kaolins (*x* and *y*) were prepared by different processes (Paper III).

Pigment	**BET** m^2/g	**Cumulative particle size distribution,** %				
		< 5 µm	< 2 µm	< 1 µm	< 0.5 µm	< 0.2 µm
GCC	12.6	99.6	94.1	70.6	42	20.3
Kaolin, *x*	22.6	99.7	97.8	96.8	89.6	47.2
Kaolin, *y*	21.2	99.5	97.4	91.6	74.6	36.3

Coating formulations are listed in *Table 3-5*. The top coat weight was 12 g/m^2 of coating with solids target at 64.5% and no on-line dilution. All coated boards were calendered by a 2-nip pilot soft calender at 50 kN/m and 150 °C surface temperature (Paper VI).

Table 3-5 Pigment compositions of coatings, in parts by weight. All coatings contained 0.15 parts polyacrylate (Ciba Chemicals), 15 parts latex (BASF), 0.5 parts carboxymethyl cellulose (CpKelco), 0.7 parts optical brightener (Bayer), 0.3 parts lubricant (Devden), and 0.3 parts cross linker (Bercen).

	G	**H**	**I**	**J**
Fine kaolin *x*	50		50	
Fine kaolin *y*		50		50
Latex *x*	15	15		
Latex *y*			15	15
Calcium carbonate	50	50	50	50

3.2 Coating capillary diameter, volume and surface area measurements

The coating porosity (incremental volume and cumulative surface area corresponding to the equivalent diameter pores) was determined by mercury porosimetry using an AutoPore IV instrument from Micromeritics. The surface tension of mercury was assumed to be 485 mJ/m^2 and its contact angle on coatings was set to 130^o according to the instrument standard. Compressions of mercury and penetrometer were included in the instrument calibrations

(Webb and Orr, 1997). It should be realized that although mercury porosimetry is widely used to characterize the pore size distributions of coatings, mercury lacks some of the basic fluid properties of coating color, paint and ink; it does not wet the coating surface and there will be no changes in coating properties due to solubility of solids, polymer/liquid interactions and variations in the capillary diameter caused by absorption. Thus capillary diameter and volume measured for the coating are more or less in their initial state when coating compression is treated as constant for the fixed ratio of pigment and latex binder in this study. Energy dispersive spectrometry (EDS) was used to measure the relative concentrations of elementals in coatings. Both mercury porosimetry and EDS measurements were conducted at analytical lab of KaMin LLC.

3.3 Contact angles with different polarity liquids

3.3.1 Binary solutions and diiodomethane for coated paper surface

There are differences between contact angles measured under static and dynamic conditions, between those measured on a flat plane and those obtained in a confined capillary (Jiang, 1979; e.g. Kistler et al. 1993), and between surfaces with pre-adsorbed film and pure dry surfaces. However, it was not possible to directly measure dynamic contact angles in the small capillaries of inhomogeneous industrial coatings used in this study. Distributions of peak pore diameters in the range 56 to 88 nm were relatively similar for all samples. Therefore, when comparing samples, the impact of capillary diameter on vapor pressure, precursor, contact angle and liquid surface tension were neglected, and the static contact angle was considered as representative of the main features also of dynamic contact angles. Coated paper samples were conditioned according to TAPPI Standard T402, and sealed in a black plastic bag before contact angle measurements. The capillary dimensions investigated were in the range 30 to 125 nm as determined by mercury intrusion. Static contact angles on coated surfaces were measured by extrapolating determination of the time-dependent contact angles to $t = 0$ s. Static contact angles at interfaces of liquid and coatings were determined by two different approaches.

In the first approach four ACCUDyneTest™ (Diversified Enterprises, Claremont, NH, USA) binary solutions (*Table 4-6*) were used in measurements with a Krüss G10 goniometer (Krüss GMBH, Hamburg, Germany). The coated paper sample was mounted with a double-sided tape on a metal base that was tilted by 1-2 degrees so that only the advancing angle was

measured. The syringe needles used had diameters of 3, 2.4, 2.4 and 1.8 mm for the 70, 60, 50 and 40 mJ m^{-2} solutions, respectively. Using such a standard surface energy series recommended by instrument manufacturer was convenient to start, also with an attempt to build a base for further studies on fountain solutions that can be a mixture of water and isopropyl alcohol etc. Drops were controlled manually by observing the drop size and curvature and then brought close to the coated paper surface. Once the attraction force pulled the drop to the paper, the needle was quickly retracted to avoid its impact on drop curvature.

Table 3-6 Composition of solutions used for dispersion and polar component calculations. Surface tensions of diodomethane (CH_2I_2, $\gamma=\gamma^d$ = 50.8 mJ m^{-2}), formamide ($HCONH_2$, γ^d = 39 and γ^p = 19 mJ m^{-2}), water (γ^d = 21.8 and γ^p = 51 mJ m^{-2}) were based on van Oss et al. (1992), and 2-ethoxyethanol ($C_2H_5OC_2H_4OH$, γ^d = 23.6 and γ^p = 5.0 mJ m^{-2}) from ACCUDyneTest™.

Solutions	**Solution compositions**					
Surface tensions, mJ m^{-2}	40	50	50.8	60	70	72.8
Diiodomethane			100%			
2-ethoxyethanol	36.5%	9.3%				
Formamide	63.5%	90.7%		65%	3.6%	
Water				35%	96.4%	100%

In the second approach the coating surface energy calculation was based on *Eqs. [2-11, -14]*, using contact angles of a polar (water) and a non-polar (DIM) solvent determined with a CAM 200 Optical Contact Angle Meter (KSV Instruments LTD, Helsinki, Finland) at the Department of Forest Products Technology, Helsinki University of Technology, Finland. The DIM was from Sigma-Aldrich, 99%. The water was de-ionized, distilled and degassed. Samples were mounted on a horizontal flat metal base with double-sided tape. Contact angles on both sides of the drop profile were measured. It was found that for all samples tested there were no statistical significances between contact angles on the two sides. Separate syringes that had fixed needle diameter were used for DIM and water. The target drop volumes were set to 7 µl for water and 1.5 µl for DIM based on the surface tension difference. After the set volume had been automatically forced out of the needles, the drop was manually brought in contact with paper as described above. The time-dependent contact angles of solution drops on each coated paper surface were measured for 10 seconds, extrapolated to $t = 0$ s and averaged from five measurements on both sides of papers.

3.3.2 Diiodomethane, formamide and water for coated board surface

Coated board surface energy calculations were based on *Eqs. [2-15,-17]*, using contact angles of a non-polar (DIM) solvent, two polar liquids (water, FMD), see *Table 4-7*, determined with the same CAM 200 Optical Contact Angle Meter at the Department of Forest Products Technology. The DIM and FMD were from Sigma-Aldrich, 99%. The water was de-ionized, distilled and degassed.

Table 3-7 Solvents used for contact angle measurements and calculations of *LW* and *AB* components of surface energy. Surface tensions of diodomethane (CH_2I_2), formamide ($HCONH_2$), hexadecane ($C_{16}H_{34}$) were based on van Oss et al. (1988). Water was based on Della Volpe and Siboni (2000).

	γ^{LW}	γ^+	γ^-	γ
Diiodomethane	50.8			50.8
Water	26.2	48.5	11.2	72.8
Formamide	39	2.28	39.6	58
Hexadecane	27.5			27.5

3.4 Ink tack measurement

It can be assumed that when a thin ink film is applied to a coating the initial concentration of the finite vehicle reservoir is the same everywhere on the surface. As the vehicle is removed by capillary imbibition, a concentration gradient is built up in the *z* direction. The vehicle concentration in the ink droplet then decreases. Ink tack builds up to the maximum, after which the ink begins to dry and tack decreases. The kinetics of ink tack force build-up may be taken as an indirect indication of the capillary imbibition process. This rate of tack build and decline was determined using a SeGan Ink/Surface Interaction Tester, in the way described by Gane and Seyler (1994). The same sheet-fed offset cyan ink (Naturallith II PC, Sun Chemical) was used in all measurements. Details are listed elsewhere (Paper VI).

4. PART A, RESULTS AND DISCUSSIONS

4.1 Pore structure characterized by mercury porosimetry

4.1.1 Pore size distribution of coated paper

Results from determinations of pore size distributions for pre-coated base paper, calendered pre-coated base paper and the six coated paper samples investigated are given in *Fig. 4-1*. The pre-coat curve from an uncalendered sample in *Fig. 4-1a* shows that the contribution to pore volume of the precoat decreases rapidly in the range above 0.125 µm. The curve for a calandered coating overlays with the pore distribution curves of all the coatings at pore sizes from ~ 0.125 down to 0.03 µm which was the cut off in order to avoid extremely high pressure. Such a high pressure can certainly cause sample structure change or even disrupt, affecting the specific Gibbs energy calculation. In this study, such a structure disruption was detected from a sharp slope change on incremental and cumulative intrusion curves, which, hence, were cut off at 0.03 µm (~ 40 MPa). These results and also the 0.65 compression ratio of calendered to uncalendered pre-coat (*Fig. 4-1a*) show that the influence of any precoat weight variation or, indeed, the base paper on the results for the total top coating must have been very limited.

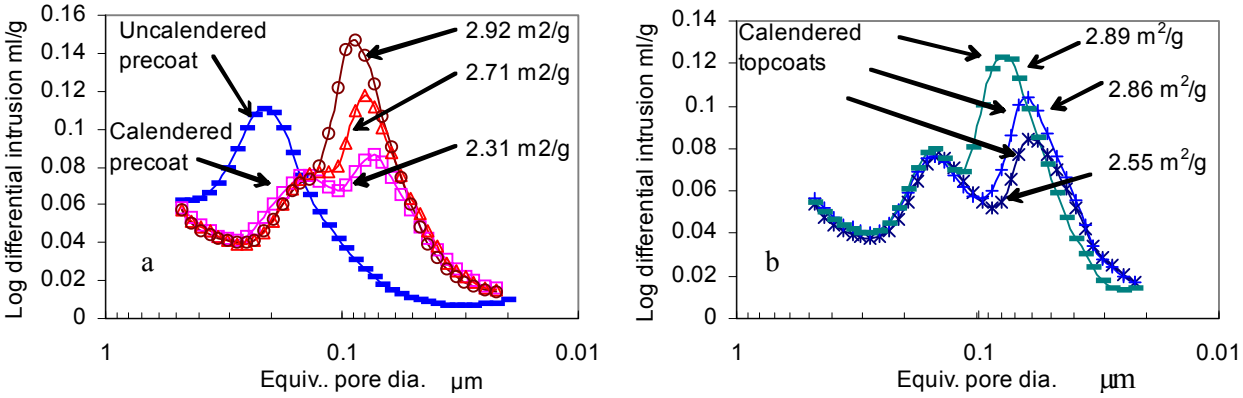

Figure 4-1a Pore size and volume reduce from uncalendered precoated paper to calendered precoated paper. At 20 parts of kaolin, for coating surface area broad GCC (A) has 2.31 m²/g; narrow GCC (C) has 2.71 m²/g; and PCC (E), 2.92 m²/g (*Fig. 4-1a*). At 40 parts of kaolin, correspondingly, (B), 2.55 m²/g; (D), 2.86 m²/g; and (F), 2.89 m²/g (*Fig. 4-1b*). For details see Paper I.

Fig. 4-2 shows results of mercury porosimetry determinations for sample C (20 parts kaolin, 80 parts narrow GCC). *Fig. 4-2a* is a conventional plot of the logarithm of differential intrusion volume *vs.* equivalent pore diameter. The large pore sizes (α) are typically due to

pores in the base paper. The shoulder (β) at medium pore sizes is mainly due to the coarse pre-coat. The peak at very small pore sizes (δ) is essentially due to the very fine top-coat. *Fig. 4-2a* shows that the topcoat contribution from small pores to the total pore volume of coatings was quite small. In contrast, *Fig. 4-2b* shows that the topcoat contribution from small pores to the total surface area of coatings was dominant. The cut-off was 0.03 µm which typically covers precoat, top coat and base paper together. Peak pore diameters and volumes are summarized in *Table 4-3*.

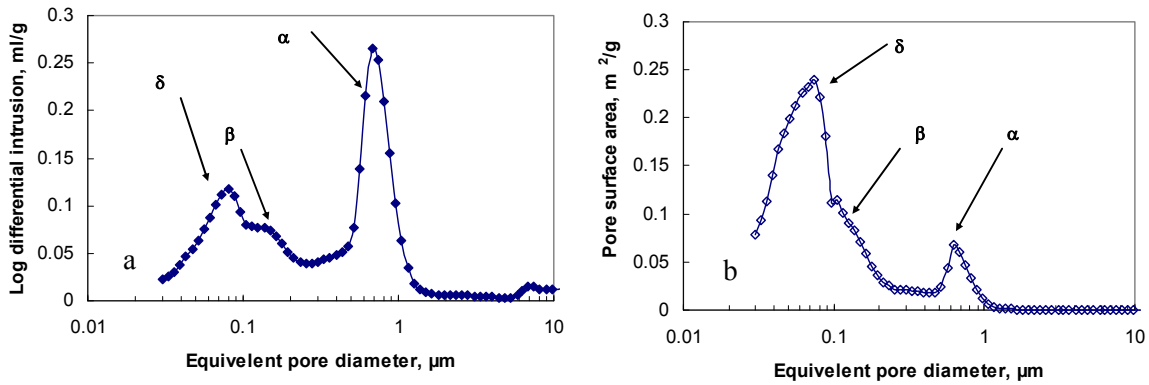

Figure 4-2*a*. *log* (differential intrusion volume) *vs.* pore diameter for Sample C determined by mercury porosimetry. *Fig. 4-2b*. Incremental pore surface area *vs*. pore diameter. Peak α is mainly due to the base paper while peak β is to the pre-coat and δ to the top-coat. Though most of the volume is located in the base paper, the pore surface area is predominantly determined by topcoat (Paper II).

4.1.2 Pore size distribution of coated board

Fig. 4-3 shows the logarithm of differential intrusion volume *vs.* equivalent pore diameter determined by mercury porosimetry for all four coated board samples. Large pore sizes around 0.25 µm are mainly due to the coarse pre-coat and the very low fraction of coarse particles from the top coat. Coatings G and H had very similar pore size and volume distributions. Coatings I and J had similar pore volume but different pore size distributions. Pore sizes and volumes of samples I and J with n-butyl acrylate-acrylonitrile- styrene copolymer were larger than those of samples G and H with styrene/n-butyl acrylate copolymer. This indicates that the different latex chemistry caused larger coating structure changes than differences between kaolin types used in this study.

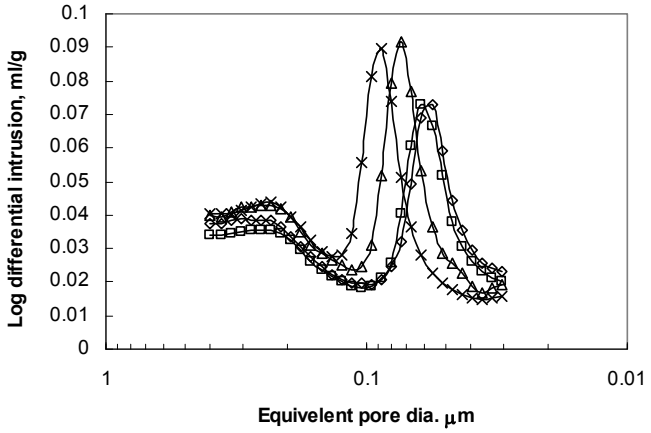

Figure 4-3 *log* differential intrusion volume *vs.* pore diameter for Coating G(◊), H(□), I(Δ) and J(x) determined by mercury porosimetry (Paper III).

4.2 Contact angles on coated paper and board

4.2.1 Contact angles on coated paper surface

An offset ink is normally a mixture of oils and pigments with dissolved or dispersed binder and additives (e.g. Leach et al. 1993). An oil based vehicle such as weak polar linseed vegetable (35 mJ m^2) or non-polar aliphatic mineral oils used in offset ink (Gane et al. 1999, Rousu et al. 2005) could also have been used. Their use would require careful standardization to achieve relevant contact angle and surface energy determinations.

In summary, the contact angles of non-polar DIM were fairly constant over a 10 s period while water contact angles required some seconds to stabilize at levels considerably lower than the initial ones. DIM contact angle differences between different kaolin levels and types of carbonates were rather small, except for sample A (20 parts kaolin) while the water differences were slightly larger at $t = 0$ s and much larger at $t = 10$ s (Paper II). The binary solution contact angles did vary significantly with the type of carbonate and kaolin/carbonate ratio (*Table 4-1*) though the contact angles for 40 mJ m^{-2} solution and DIM were more or less within experimental error the same for all coatings.

Table 4-1 Initial contact angle θ at t = 0 s of the coated paper samples with standard error σ of five measurements determined with the CAM 200 (DIM and water) and Krüss G10. Compositions of samples A-F are given in *Table 3-2*. (Paper II).

Solution	**Contact angle and standard error** Degrees											
	A		**B**		**C**		**D**		**E**		**F**	
	θ	σ	θ	σ	θ	σ	θ	σ	θ	σ	θ	σ
DIM (50.8 mJ m^{-2})	52.0	0.9	47.4	1.7	49.8	1.9	48.6	2.3	48.3	2.1	50.6	2.0
Water (72.8 mJ m^{-2})	95.0	1.4	91.1	1.9	93.3	1.4	85.6	2.1	90.7	2.7	86.6	0.9
40 mJ m^{-2} solution	27.5	0.6	28.2	1.9	27.1	1.0	25.8	1.2	25.6	1.0	26.9	0.4
50 mJ m^{-2} solution	65.9	0.5	55.1	1.3	50.8	1.7	48.5	0.7	53.5	1.8	47.5	1.5
60 mJ m^{-2} solution	65.8	1.2	58.8	0.1	59.9	1.3	57.5	0.2	61.6	1.7	58.4	0.6
70 mJ m^{-2} solution	69.0	0.6	62.0	2.1	59.2	1.0	54.9	1.3	58.4	0.4	55.3	0.3

When the kaolin increased from 20 to 40 parts by weight the initial contact angle of water decreased regardless of the type of calcium carbonate used. This indicates that as kaolin level increased, the coating was more hydrophilic. It is also true for the solutions with surface energy 50, 60 and 70 mJ m^{-2}; for the 40 mJ m^{-2} solution the contact angle was more or less constant within experimental errors. Kaolin, with the general formula $Al_4Si_4O_{10}(OH)_8$, is aluminosilicate with 7 Å repeat units of 1:1 tetrahedral silicate and octahedral alumina sheets with hydroxyl groups located between tetrahedral silicate layers that are very stable with dipole moments balanced between silicon and oxygen pairs. Thus, a kaolin particle has both siloxanol and aluminol surfaces. The hydroxyl-covered surfaces are hydrophilic. Hence, additions of more kaolin at the expense of carbonates are expected to render the coatings more hydrophilic. The magnitude of the van der Waals component, γ^{LW} in oxide materials, including clay minerals, typically varies between 35 and 45 mJ m^{-2} (van Oss et al. 1992).

Using *Eq. [2-11,-14]* to calculate polar and non-polar contributions, coating surface energies ranged between 30-40 mJ m^{-2} at t = 0 s. Carbonates, kaolin, and latexes such as styrene butadiene and acrylate latexes can change the mean polar surface energy component of the coatings. The surface energies of major latexes used in paper coatings are 40–65 mJ m^{-2} (Kan et al. 2004). The fact that coating energies calculated from t = 0 s were lower than those of kaolin but were in the range corresponding to latex indicates that latex surface energy is important. Hence, modification of latexes can affect coating surface energy and, in turn, the

Gibbs energy and ink tack development. Indeed, this is the case when latex chemistry was changed as discussed in the following (Paper III).

4.2.2 Contact angles on coated board surface

It is interesting to note that DIM contact angles on latex *y* coatings were higher than those on latex *x* coatings while there was little difference of contact angles between kaolin *x* and *y* (*Fig. 4-4*). All contact angles of DIM tended to decrease as a function of time between $t = 0 – 10$ s with the contact angles on latex *y* coating that started at higher values decreased faster than those on latex *x*. Because of the non-polar nature of DIM the contact angle and rate of decrease differences are particularly important for the study of polymer influence on Gibbs energy in ink oil imbibition.

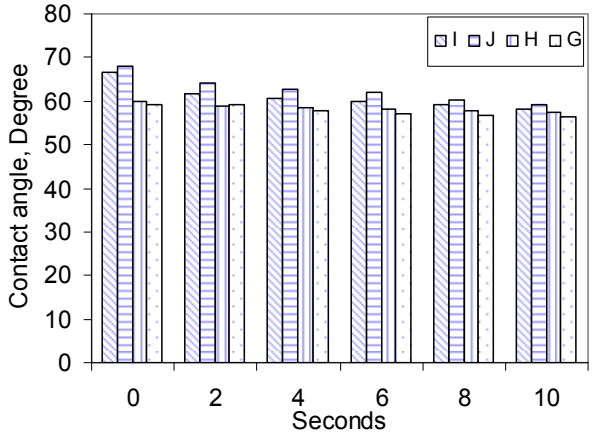

Figure 4-4 Contact angles of DIM on coating *G* and *H* containing styrene/n-butyl acrylate, and *I* and *J* containing n-butyl acrylate-acrylonitrile- styrene. The contact angle decreased as a function of time at different rate between the two different polymers between $t = 0 – 10$ s (Paper III).

Extrapolated values of contact angles with standard deviation are given in *Table 4-2*. In fact, all liquids except hexdecane contact angles on latex *y* coatings were higher than those on latex *x* coatings. The standard deviations were rather high for all the liquids tested except for hexdecane, implying that the differences between contact angles of DIM and FMD on coatings *G* and *H* are not statistically significant. The same is valid for the difference between *I* and *J*.

Table 4-2 Initial contact angle θ at t = 0 s of the coated board determined with the CAM 200 (DIM, water, FMD and Hexadecane). σ = standard deviation.

	G		H		I		J	
	θ	σ	θ	σ	θ	σ	θ	σ
DIM	59.3	2.9	59.8	3.5	66.6	4.1	67.9	5.5
Water	86.4	2	92.8	2.4	90.3	6.3	95.5	5.9
FMD	74.4	3.7	72.8	4.4	84.1	5.9	85	3.9
Hexadecane	20.1	1.0	20.4	2.5	19.6	2.1	20.5	1.0

The acid (electron acceptor) parameter γ^+ is generally small or negligible although this at least partially depends on the choice of standard values of $\gamma^+$and γ^- of water (Della Volpe, Siboni 2000). Major variations exhibited by oxides lie in the base (electron donor) contribution, γ^-, with values ranging from 3 – 80 mJ m^{-2} (van Oss, Good 1995). Thus, the value to a large extent decides the balance between hydrophilic and hydrophobic properties of clays such as kaolin, talc, muscovite mica, smectite etc. Kaolin has γ^- values between 30-35 mJ m^{-2} and total surface energies in the range of 65-80 mJ m^{-2}, as determined by thin-layer wicking method (Wu 2001).

4.3 Calculations of Gibbs energy

As an example of paper coating, the individual pore diameters with the corresponding incremental specific pore volumes from mercury intrusion were used to calculate the change in Gibbs energy for each incremental volume, using the solution surface tension (40 mJ m^{-2}) and the contact angles given in *Table 4-1*. These incremental energies were then summarized to give the total change in ΔG_s (*Eqs. [2-9, -10]*). The results are summarized in *Table 4-3*.

Table 4-3 Pore surface area, Specific Gibbs energy (ΔG_s), specific pigment surface area, peak pore diameter and volume and time to reach maximum ink tack (t_{max}) for investigated paper coatings. ΔG_s was calculated for pore size range 0.03-0.125 μm. The pigment surface area was calculated based on the areas of the individual pigments in *Table 3-1* and the pigment ratio (Paper I).

Sample ID	**A**	**B**	**C**	**D**	**E**	**F**
Pigment composition	20 kaolin+ 80 B GCC	40 kaolin+ 60 B GCC	20 kaolin+ 80 N GCC	40 kaolin+ 60 N GCC	20 kaolin +80 PCC	40 kaolin +60 PCC
Surface area (m^2/g)	2.31	2.55	2.71	2.86	2.92	2.89
ΔG_s (mJ/g)	-411	-452	-485	-526	-527	-523
BET area (m^2/g)	14.3	16.0	15.2	16.7	13.9	15.7
Peak pore diam. (μm)	0.073	0.056	0.080	0.061	0.088	0.080
Peak pore vol. (ml/g)	0.086	0.085	0.118	0.104	0.147	0.123
t_{max}, (s)	55.3	44.6	36,4	31.4	22.3	23.6

Details with step-by-step calculation are given in *Table 4-4*. The specific incremental pore volume was taken from the intrusion volume of mercury into a known mass of intact coated paper sample (0.6848 g sample weight for Sample A) multiplied by a coat weight factor corresponding to a lab-determined basis weight of the sample (110.8 g/m^2 for Sample A) divided by the (12 + 12) g/m^2 constant top coat weights. Data in *Table 4-3* are mainly based on mercury intrusion and BET analytical results. The quality is ensured by strictly following KaMin analytical procedures. For this study, two samples are analyzed and averaged. If they are not close to each other based on the author and analytical chemists' experience. A third sample is tested. The NSOM and AFM of Paper IV follow the same way. Standard deviation is not suitable for such a small sample population.

Table 4-4 Details of Specific Gibbs energy calculation for the pore at 0.03- 0.125 μm of Sample A.

Step One	**Calculation of constant C for one coating** **The C=4γcos(θ)BW/CW mN/m calculation**		
	Surface tension,γ	40	mN/m
	cos(θ)	0.8870	
	cos(θ) γ	35.5	mN/m
	Total basis weight	110.8	g/m^2
	Top coat weight C2S	24	g/m^2
	C	655	mJ/m^2

Step Two	**Select Pore dia. as Dia. and Incremental pore volume as ΔV** **The ΔG_s =C*ΔV/D mJ/g calculation**		
No. ith equivelent pores	Pore Diameter (μm)	Incremental Pore Volume (mL/g)	ΔG_{si}
1	0.125	0.0029	-15.3
2	0.114	0.0027	-15.6
3	0.105	0.0026	-16.1
4	0.096	0.0026	-17.6
5	0.088	0.0028	-20.6
6	0.080	0.0032	-26.0
7	0.073	0.0034	-30.4
8	0.067	0.0033	-32.5
9	0.061	0.0030	-32.4
10	0.056	0.0027	-31.8
11	0.051	0.0023	-29.9
12	0.047	0.0020	-28.0
13	0.043	0.0018	-27.3
14	0.039	0.0013	-22.4
15	0.036	0.0014	-26.1
16	0.033	0.0010	-20.7
17	0.030	0.0009	-18.7
Step Three	**Sum up Gibbs for all pores with corresponding volume**		
	The $\Delta G_{s(0.03\text{-}0.125)}=\Sigma\Delta G_{si}$	-411.4	mJ/g

Example of Sample A					
Pore Diameter (μm)	Incremental Pore Volume* (ml/g)	Surface tension (mJ m^{-2})	Contact angle (°)	$\Delta G_{s0.125}$ (mJ/g)	$\Delta G_{s0.03\text{-}0.125}$ (mJ/g)
0.1250	0.00292	40.0	27.5	-15.3	-411

Table 4-4a A complete set of trial results with the inclusion of 100% broad GCC and narrow GCCs, and 100% PCC that are rarely used in practice as a sole pigment but of fundamental interest. B GCC = Broad GCC, N GCC = Narrow GCC, and *R* is correlation coefficient.

	100 B GCC	20 kaolin+ 80 B GCC	40 kaolin+ 60 B GCC	100 N GCC	20 kaolin+ 80 N GCC	40 kaolin+ 60 N GCC	100 PCC	20 kaolin +80 PCC	40 kaolin +60 PCC	***R*** with t_{max}
Gibbs energy, mJ/g	-335	-411	-452	-408	-485	-526	-482	-527	-523	-0.92
Peak pore dia.) m	0.105	0.073	0.056	0.105	0.08	0.061	0.104	0.088	0.08	-0.26
Peak pore V, ml/g	0.104	0.086	0.085	0.1334	0.118	0.104	0.171	0.147	0.123	-0.50
BET, m^2/g	12.6	14.3	16.0	13.7	15.2	16.7	12.1	13.9	15.7	-0.35
t_{max}, s	100	55	45	46	36	31	23	22	24	

4.4 Liquid surface energy and polarity influence on Gibbs energy

For all liquids (*Table 4-1*) tested on coated paper except DIM and the solution with surface tension 40 mJ m^{-2}, the differences between $\gamma cos\theta$ of different coatings were statistically significant. The 50 mJ m^{-2} solutions combine 90.7% of FMD with 9.3% of EO. The dipole moment of FMD is very large, about 3.7 Debye (Israelachvili, 1991). The EO is surface active, *i.e.* the surface tension is lowered when it is dissolved in FMD, due to the strong cohesive forces in FMD. The 60 and 70 mJ m^{-2} solutions have 65% and 3.6% FMD combined with 35% and 96.4% of water, respectively. FMD has a strong tendency to form hydrogen bonds with kaolin surface and to intercalate (Wada 1961) kaolin stacks. FMD intercalation into kaolin always starts from the edge and the rate can increase significantly with addition of some water (Olejnik et al.1970; Franco, Ruiz Cruz 2004).

All these intermolecular forces and reactions occurring in binary solutions and at liquid-solid interfaces make the interpretation and comparison of contact angles for different solutions and coatings quite complex, as evident from the results given in *Table 4-1*. This observation confirms that combining rules for surface energies and adhesion may not be valid for interfaces in systems with more than two components at an interface (Good 1992). Still, the good match of ΔG_s from surface tension 40 mJ m^{-2} to t_{max} shows that a selection of binary solutions that do not contain substantial fractions of strongly polar solvents may still be used for Gibbs energy calculation. ΔG_s calculated from strongly polar solutions will be applicable for studies of interactions between polar substrates and polar solutions, such as kaolin-containing coatings and aqueous fountain solution used in lithographic printing, and solutions used in flexographic printing. Emulsified ink study has been completed and will be reported in due course.

The 50 mJ m^{-2} solution and DIM had similar surface tensions but interacted differently on penetrating into coatings (*Table 4-1*). Non-polar DIM interacts with all components in coatings but predominately through dispersion interactions. The solution surface tension reflects intermolecular interactions between liquid molecules while the penetration into coating is determined by the liquid-solid-vapor interface. It is concluded that in the interactions of polar solution with a polar coating surface, the solution polarity plays an important role in determining Gibbs energy. Differences in capillary sorption of solvents with

similar surface tension but different polarity such as ethylenglycol and glycerol were observed by Gane et al. (1999).

4.5 Latex and kaolin chemistry influence on coating surface energy

The values of acidic component are very low (*Table 4-5*), and as a whole *AB* component of surface energy is so low that the influence of acid-base interactions can be more or less neglected when compared to *LW* forces in coatings. Although the general trend that *LW* components accounts for the major part of total surface energy on coated board is in accordance with our previous study on coated paper, there is a key difference between the results presented here and the earlier ones. In contrast to the coated paper study with fixed latex, the value of *LW* component of these coated board surfaces changed when latex type was changed and so did the base parameters and ΔG_s, to be discussed below.

Table 4-5 Coated board surface energies calculated from *Eqs. [2-15, -17]*. Ink tack developments were measured on ISIT and calculated from a linear differential equation model (Paper III).

	G	**H**	**I**	**J**
γ, mJ m^{-2}	29.3	29.4	25.9	24.5
γ^{LW}, mJ m^{-2}	29.0	28.7	24.8	24.1
γ^{+}	0.01	0.15	0.08	0.03
γ^{-}, mJ m^{-2}	3.0	0.9	3.4	1.8
γ^{AB}, mJ m^{-2}	0.3	0.7	1.0	0.4
Time to reach max. tack, t_{max}, s	11	15	17	23
Max. tack force, F_{max}, N	7.3	7.2	6.1	5.8
Final tack force, t = 300 s, N	0.79	0.80	0.41	0.48

The *LW* components of kaolins G and H are similar. This can be traced back to where they were mined, *i.e.* from the same geological site. However, the base parameter of kaolin *y* was lower than that of kaolin *x*. Given the fact that there was a very small difference in surface area determined by BET (*Table 3-4*), the origin of such a large base parameter difference may be the bulk mineral composition but it seems more reasonable to assume that it is due to surface chemistry modification in the processing of the kaolin. Effective utilization and conversion of the octahedral surface hydroxyls to change surface chemistry by chemical adsorption from simple cations to complex polymers has been a major subject in kaolin surface chemistry modifications for coating, ink, rubber, plastic applications, to name only a few. The background of working on octahedral instead of tetrahedral can be basically

illustrated by a theoretical study in which quantum chemical calculations within the framework of a very basic octahedral-tetrahedral 1:1 kaolin crystal structure demonstrates that carboxylate group of acetate bound to the octahedral surface hydroxyls via hydrogen bridge mechanism, and its interaction energy amounts to -292.9 kJ/mol. On the other hand, the acetic acid molecule interacts with tetrahedral surface through weaker hydrogen bonds, and the adsorption energies are only about -16.7 kJ/mol (Tunega et al. 2002).

Switching latex changed both *LW* and base parameter levels. While the use of latex *y* certainly reduced *LW* interactions, compared to latex *x*, it increased the coating base parameter slightly. For acrylate-containing latex, the type involved in this study, the size of alkyl group can affect both dispersive (*LW* component in oil imbibition) and polar surface energies. Changing from iso-octyl acrylate to ethyl acrylate results in a dispersive component decrease from 43.7 to 22.1 mJ/m^2 and an increase of the polar component from 0.1 to 16.7 mJ/m^2 (Chan, Van Gilder 2004). Functional group introduction into a polymer chain and/or to a chain end can significantly change polymer surface energy (Tsibouklis et al. 1999).

The surface concentration of polymer will affect the coating surface energy. The major difference between latex *x* and *y* according to their material safety data sheets (MSDS) is that latex *y* contains acrylonitrile (C-C-C≡N) group. However, energy dispersive spectrometry (EDS) measurements (*Fig. 4-5)* shows that no nitrogen is detected near surface at low energy level of 7.5 kV while the latex carbon (lighter element than nitrogen) level is strong (a small part from $CaCO_3$). It is reasonable to conclude that acrylonitrile group concentration on surface is much lower than that of the hydrocarbon in the backbone, and thus, the surface energy change can be attributed to a combination of other polymer chemistry, structure changes, and acrylonitrile groups etc. We note that although the very low acrylonitrile concentration on surface makes it less important to *LW* interactions, the polar moieties orientation under the influence of polar liquid cannot be ignored when *AB* interactions are involved (Adamson, Gast 1997).

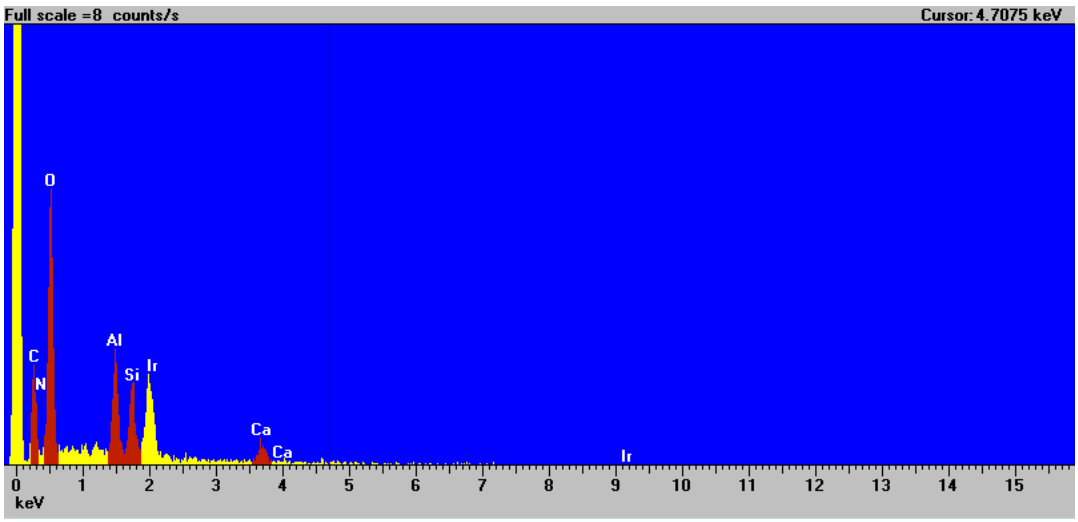

Figure 4-5 The key element analysis on coated sample I containing acrylonitrile (C-C-C≡N) group by energy dispersive spectrometry (EDS) at 7.5 keV (Paper III).

4.6 Gibbs energy and ink tack kinetics

4.6.1 Ink tack on coated paper

The ink tack force development as a function of time is shown in *Fig. 4-6*. Interestingly, t_{max} are very different for different carbonates and different levels of kaolin in paper coatings though the maximum tack forces, F_{max} are very similar.

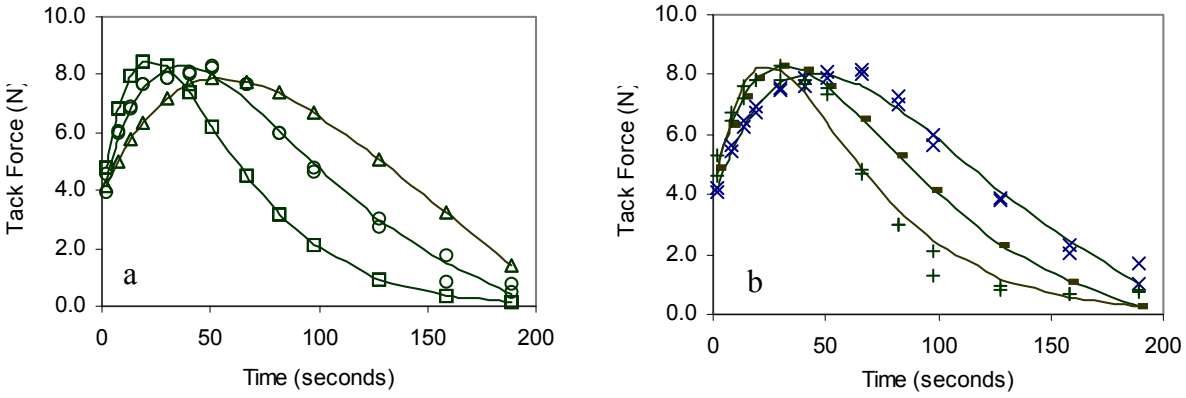

Figure 4-6a. Results from ink tack measurements for coatings A (Δ), C(o), and E (□) of 20 parts kaolin, and 5-6b B(x), D (-), F(+) of 40 parts kaolin with broad GCC, narrow GCC and PCC, respectively (Paper I).

4.6.2 Ink tack on coated board

Fig. 4-7 compares ink tack development on the four board coatings. Notably, coating I (with n-butyl acrylate-acrylonitrile-styrene latex) produced a lower maximum tack force F_{max}, needed longer time (t_{max},) to reach F_{max}, and yielded a lower final tack force after t = 150 s than coating G (with styrene/n-butyl acrylate latex). The same held true for coating J relative to coating H. Compared to coating G with kaolin *x*, the H with kaolin *y* had the same F_{max} and final tack force, but different t_{max}, *i.e.* the t_{max} of coating H with kaolin *y* was longer than that of coating G with kaolin *x*. Similar differences were observed between coatings I and J.

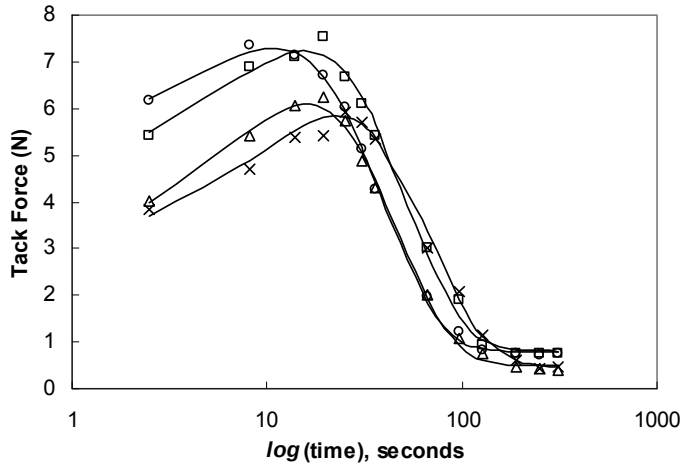

Figure 4-7 Tack force *vs.* time for coating G (o), H (□), I (Δ) and J (x) on log-linear scale. The curves feature time to reach the maximum tack, t_{max}, the maximum tack force (peak force value), F_{max}, initial slope, and final tack force (the last point of testing) in Paper III.

For the type of paper coating formulations shown in *Fig. 4-1*, the coating structure is bimodal, with one of the peaks occurring at pore size less than 0.1 μm. Comparison of the t_{max} for these coating to the pigment BET surface area of the different pigment blends (*Table 3-1*) and peak pore diameter shows very little correlation (R^2= 0.12 and R^2= 0.07, respectively) between these quantities. There is a very weak correlation, R^2= 0.75 (R= -0.87), between peak pore volume and time to maximum tack force (Paper I). *Table 4-4a* summarizes correlation coefficients of ink tack to pigment areas, diameters, peak pore and volume, and ΔG_s. As shown in *Fig. 4-8*, there is a strong correlation, R^2=0.94 (R=-0.97), between the ΔG_s calculated from the pore size range of 0.03 – 0.125 μm and t_{max}. It is recorded that the shape of pores - sharp dislocations in particular caused by pigment packing, can have a bigger effect on liquid imbibition than pore size in certain cases (Senden et al. 2000). The lower correlation

coefficient R = -0.92, when 100% broad and narrow GCCs, and 100% PCC are included in the same coated paper study (*Table 4-4a*), can be partially attributed to such pore shape differences. The surface porosity quantification and spatial variation in surface porosity can also have effects (Chigna, Helle 2003).

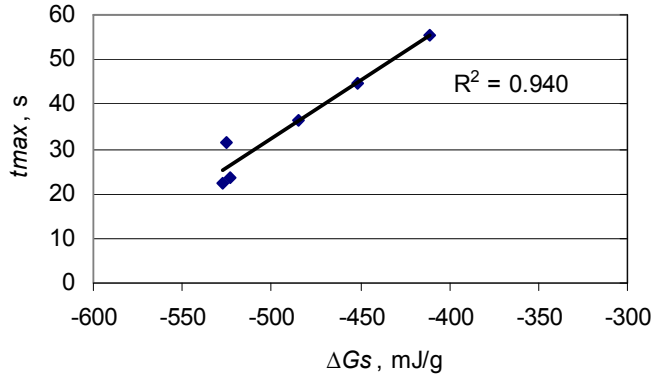

Figure 4-8 Correlation of t_{max} with specific Gibbs energy (Paper I).

A simple argument to explain the correlation to Gibbs energy would be the following. The surface tension in a capillary giving rise to the capillary pressure is a driving force that causes wetting liquids to penetrate spontaneously into capillaries. Thermodynamically, this implies that imbibition will lead to a lowering of the Gibbs energy. The driving force will be larger, the larger the difference in pressure between the source liquid and the liquid in the capillary, *i.e.* the larger the gradient in Gibbs energy. Thus, in the absence of activation energies, which would strongly impede the flow, a capillary with a given diameter (or a coating with a given pore size and volume distribution) will fill faster with a given liquid, the lower the Gibbs energy of the liquid in the capillary (*Eqs.2-1, -4*). This would imply that there should be a correlation between the Gibbs energy calculated in the way described and t_{max} and *Fig. 4-8* demonstrates such a relationship does exist.

There are other forces, such as hydrodynamic factors (*Eq. [2-8]*) that come in play in the rate at which ink vehicle is taken into the coating, and one needs to include these forces in a full evaluation. The LW equation describes the balance of some hydrodynamic forces as the ink vehicle is imbibed, *i.e.*, the balance between the capillary pressure as the driving force for adsorption and the internal friction (viscosity) as a retarding force. A direct evaluation based on LW equation would predict that penetration will be the faster with larger capillary radii and with larger the liquid surface tension. As noted in the introduction, in the initial stage the

inertia force and kinetic energy will actually qualitatively turn this prediction around, *i.e.* initially a capillary will fill faster, the smaller the cross-sectional area of the capillary. Previous studies (Zhmud et al. 2000; Stange et al. 2003) have successfully modeled and experimentally verified three phases. They are the initial stage in which the rate is proportional to t^2, a short transition period where the rate is proportional to t, and third phase where the rate of filling of the capillaries does actually depend linearly on $t^{(1/2)}$, as qualitatively predicted by the LW equation. Furthermore, other retarding forces, such as local transient sticking of the ink vehicle at the surface asperities or chemical inhomogeneities and capillary topography and connections/throats between capillaries in a heterogeneous porous medium affect the total rate of imbibition. In addition, the rate of filling is often much lower than that predicted, due to thickening of the ink as liquid drains from it (Schoelkopf et al, 2003a, 2003b). However, none of these resistant factors will change the fact that the basic force that drives spontaneous imbibition is the capillary force/gradient in Gibbs energy. And so, irrespective of the retarding forces it seems reasonable that the total flow rate should increase when this overall force increases. *Eq. [2-9]* gives a measure of the driving force (the gradient of the Gibbs energy) over the whole assembly of capillaries in heterogeneous porous coatings when all capillaries that are filled at the maximum pressure used in mercury porosimetry.

This thesis therefore proposes that $\Delta G_{s,}$ which can be calculated directly from porosimetry data, liquid surface tension and contact angle may offer a basic and convenient way to characterize a porous coating structure and interaction of surface energies, and can be used to predict how offset inks will be imbibed into the coating. Of the other quantities listed in *Table 4-3* (Paper I for details) none is directly connected to the driving force of imbibition in the same way, which explains that they are not correlated to t_{max}. The initial rate of tack rise is another property often used to characterize ink setting in coating. As already noted, there will be a strong influence of inertia force and kinetic energy on the initial penetration into capillaries, and conditions will therefore be quite different from those in liquids mainly driven by the equilibrium capillary pressure. Hence, though the driving force is the same there should be a weaker correlation of the initial rate of penetration to the ΔG_s as calculated here, and our investigations have indicated that such is, indeed, the case ($R^2 = 0.72$).

4.7 Coating structure and surface energy influence on coated paper

Gibbs energies based on contact angles of DIM drops on coating and the mercury porosimetry results were calculated from *Eq. [2-9]*, and compared to t_{max}. A reasonably linear correlation (*Fig. 4-9*, R = -0.92) was found though it was weaker than correlations obtained previously for the 40 mJ m^{-2} solution (R = -0.97).

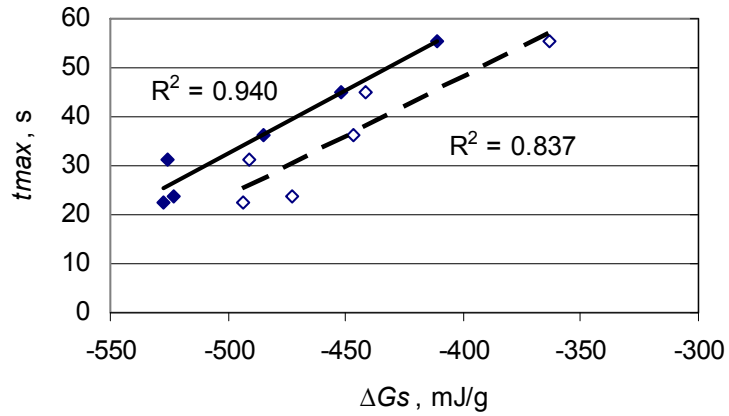

Figure 4-9 Correlations of t_{max} with specific Gibbs energy ΔG_s, ◇ and dash line: DIM; ◆ and solid line: 40 mJ m^{-2} binary solution (Paper II).

The surface interactions between a mainly non-polar offset ink and the coatings are obviously expected to mainly due to the dispersive components in the surface tension. This can also be mathematically analyzed. *Eq. [2-9]* can basically be seen as a product of a coating structure variable, $\sum(V_i/D_i) = \sum \pi D_i h_i$ and a surface energy parameter, $\gamma cos\theta$. Differences in the surface interactions will turn up as variations in the latter parameter. To identify the significance of means of sample strips that are statistically different from the mean of the control, taking sample C as control and applying Dunnett's multiple comparison procedure in Analysis of Variance, ANOVA (Dunnett 1964) to the contact angle variations, assuming the surface tensions of each liquid in *Table 3-6*, it was found that the $\gamma cos\theta$ differences between the six samples, using the 40 mJ m^{-2} solution were statistically insignificant, *i.e.* $\gamma cos\theta_{comparison} - \gamma cos\theta_{control}$ fell within the limits of experimental uncertainty for coatings with different levels of kaolin and type of carbonates (*Table 4-6*). The same was true for DIM. Therefore the large Gibbs energy differences (-411.4 to -527.1 mJ/g for 40 mJ m^{-2}, and -363.0 to -493.7 mJ/g for DIM, *Fig. 4-9*) were mainly determined by the coating structure variable. This demonstrates

the strength of the Gibbs energy approach in being a parameter that is able to distinguish between the influence of surface interactions and the influence of structural properties on capillary adsorption.

Table 4-6 Differences of surface energy parameter, $\gamma cos\theta$ calculated from Dunnett's multiple-comparison with a control (sample C). The 95% confidence limit was calculated from the numbers of coatings and contact angle observations, and the estimate of variance σ^2. Statistically insignificant differences are given in bold *Italics* (Paper II).

	$\gamma cos\theta$ **differences based on Dunnett's procedure** mJ m^{-2}						
	C	A	B	D	E	F	Limits
40 mJ m^{-2} solution	*	***0.1***	***0.4***	***0.4***	***0.5***	***0.1***	***±0.71***
50 mJ m^{-2} solution	*	-11.2	-3.0	1.5	-1.9	2.2	±1.97
50.8 mJ m^{-2} DIM	*	***-1.5***	***1.6***	***0.8***	***1.0***	***-0.5***	***±2.05***
60 mJ m^{-2} solution	*	-5.5	1.0	2.1	-1.6	1.3	±1.73
70 mJ m^{-2} solution	*	-10.8	-3.0	4.4	0.8	4.0	±2.29
72.8 mJ m^{-2} water	*	-2.2	2.8	9.8	3.3	8.5	±3.75

The specific Gibbs energy, ΔG_s associated with imbibition of a solution into a porous coating (*Eq. [2-9]*) can be basically treated as a product of coating structure variable, $\sum(V_i/D_i)$, and surface energy parameter ($\gamma cos\theta$), *i.e.* ΔG_s highlights the interactive properties of the coating pore surface and the probe liquid. In mixed kaolin/carbonate coatings, increasing the fraction of kaolin renders coatings more hydrophilic. Thus, one expects relatively strong interactions of coatings containing kaolin with aqueous test liquids, and with aqueous fountain solutions, flexo and ink-jet printings, and UV varnishing. However, coating hydrophilicity affects the imbibition of non-polar solvents much less than the coating structure variable, $\sum V_i/D_i$. For non-polar solvents this variable is of predominant importance for ΔG_s, and thus, in turn, governs t_{max} of inks based on non-polar solvents. When dispersive energy is relatively constant (which is the case for the coating pigments used in paper coating study) and dominant at the liquid-solid-vapor interface, the coating structure decides the differences in ΔG_s and t_{max}. This agrees with chromatographic results, which demonstrates that the removal of slightly polar linseed oil is retarded by non-polar mineral oil (Rousu et al. 2000, 2005), and with the post treatment of coating with silane in super-critical CO_2 which

shows the surface hydrophobicity plays a minor role in controlling offset ink setting (Gu et al. 2007).

4.8 Coating structure and chemistry influence on coated board

Coated board has higher binder level and rougher surface than coated paper. Such chemical composition and surface topography affect ink and coating interactions. Therefore it deserves separate discussions. Results in *Table 4-7* demonstrate the utility of ΔG_s as a relevant parameter characterizing ink tack development properties of coatings. Though four points are not sufficient for a full statistical analysis, it can be concluded from *Table 4-7* that the lower $\sum(V_i/D_i)$ tended to correlate with the longer t_{max}. While this is in agreement with our previous studies (Paper I and II), it is emphasized that a higher value of surface energy parameter $\gamma cos\theta$ at interface measured with non-polar solvent DIM resulted in a shorter t_{max}.

Table 4-7 Summary of time to reach maximum tack, structural variable, surface energy parameter at interface and Gibbs energy of imbibition (over pore size range of 0.03 - 0.195 μm) of all four coatings, determined by using diiodomethane (Paper III).

	G	H	I	J	Correlation, *R*
t_{max}, s	11	15	17	23	
$\sum V_i/d_i$, m^2	11.5	11.0	11.2	9.9	0.94
$\gamma cos\theta$, mJ m^{-2}	25.9	25.6	20.2	19.1	0.88
ΔG_s, mJ/g	1202	1127	903	754	0.96

Surface energies of polymers have earlier been characterized in terms of dispersive and polar interactions (Wu, 1982). This approach was extended to the use of polar to total surface energy ratio, γ^P/γ, and it was found that the higher γ^P/γ, the lower the oil-based ink setting rate (Van Gilder, Purfeerst 1994). In our study γ^{AB}/γ is not correlated to t_{max} possibly due to the very low γ^{AB} determined at t = 0 s. On the other hand, the correlation of γ^{LW} and γ with t_{max} is rather consistent. This is not surprising because the coating surface energy, γ is mainly determined by γ^{LW} (*Table 4-5*), and dispersive forces are predominant in the ink oil imbibition into porous coatings. It is noted that this study directly characterizes coated board surface and pore structure with liquids while the previous study characterizes latex film with liquid contact angles, and inverse gas chromatography (IGC) in the Henry infinite dilution region. It has been suggested that IGC mainly assesses the high energy sites (Jacob, Berg 1994).

It is recognized that there is the complexity of contact angle hysteresis that has been a major subject in surface wetting in air and liquid environments (e.g. Marmur 1996, 2004), and spreading of wetting line advances through kinetic and dynamic balances (Shanahan, 2001). Because of the small capillaries of inhomogeneous industrial coatings and variety ingredients of inks, in practice the Gibbs energy was calculated from measurements of drops of pure liquids of known surface energy on coated paper and board surfaces, assuming smooth, non-deformable and non-absorptive surfaces. As is well known, the penetration of liquid over irregular surfaces or into complex structures may be intermittently arrested by sticking of the liquid at sharp edges or notches. The present study does not take this possibility in to account. Paper surface roughness effects on water drop spreading have been discussed in the literature (e.g., Modaressi, Garnier 2002; Werner et al. 2005). Indeed when fine oblate spheroids are used in coating, due to particle alignments under a shear field, the surface should be characterized as centerline average, *rms,* correlation length and autocorrelation as described in **Part B** (Paper IV). Furthermore, such fine oblate spheroids introduction can cause chemical distribution change in dewatering and evaporation processes, in addition to the coating structure change in thickness direction as illustrated in **Part C** (Paper V). That the absorption of drops could be neglected in contact angle measurements is ensured by extrapolation of time-dependent contact angles to $t = 0$ s. This method is related to the front line of the advancing contact angle in capillary adsorption. If coating components, latex lattices in particular, swell during ink setting, as proposed in previous studies (Van Gilder, Purfeerst, 1994; Xiang et al. 2004), the proposed method may oversimplify latex and solvent interactions that are due to physisorption and/or chemisorption as a function of time. So far, no difficulties have been encountered by using contact angle at $t = 0$. This implies that due to the limit imposed by rheology coating ingredients are designed to be compatible, less strong polar interaction for example (Van Gilder 2004), and as such, this treatment is justified by those coating properties studied, and by the dispersive force predominance (loosely defined as phyciosorption) in coating and oil-base ink interactions.

5. PART A, CONCLUSIONS

The coating structure characterized by mercury intrusion and contact angle extrapolated to t = 0 s may be used to calculate the total Gibbs energy of capillary imbibition into a heterogeneous porous medium of a given liquid at the final state. The good match between the time needed to reach the maximum tack force (t_{max}) and the specific Gibbs energy (ΔG_s) leads to the conclusion that though many factors affect the capillary imbibition in the initial state and rate of access to the final state, the calculation of ΔG_s from the coating structure determined by mercury porosimetry and surface energy at the liquid-solid-vapor interface appears to reflect the effect of coating structure and surface energy on imbibition of ink until maximum tack is reached better than other characteristics often used. The application of *Eqs. [2-9,-10]* to current popular top coating systems shows that a larger capillary pore surface area strongly increases the rate of ink setting, as measured by the reduced t_{max}, while there is no correlation between ink tack development and pigment surface area or peak pore size of the coating. A larger pore volume in a coating structure tends to reduce t_{max}, but the correlation is weak, at least for the coatings used in this study.

The results further demonstrate that the Gibbs energy concept combining coating structure variables (volume and diameter, $\sum(V_i/D_i)$) and surface energy parameters ($\gamma cos\theta$) at the interface is a better method for characteristics of capillary adsorption than each parameter alone. Indeed, the change in latex chemistry contributes to both coating structure and surface energy changes. In both kaolin and latex cases the base parameters γ^- (in the vOCG approach) were low compared to Lifshitz-van der Waals interactions, γ^{LW} while the acid γ^+ component was negligible. Furthermore, the designed kaolin with constant γ^{LW} and different γ^- changed the ΔG_s, and coated paper capillary adsorption in offset ink setting, as seen in the different t_{max} but there was no effect on the maximum tack force, F_{max} and the final tack. Compared to styrene/n-butyl acrylate latex, n-butyl acrylate-acrylonitrile-styrene latex that lowered γ^{LW} on coated board surface and ΔG_s significantly increased t_{max}, and reduced F_{max} and the final tack.

So far, the successful applications of Gibbs energy concept has been demonstrated in the analysis of interactions of oil-based offset ink with porous coatings that have different contents of calcium carbonates, kaolin and latex. It is expected that such an approach may find applications in analyzing interactions of different porous coatings with polar and non-

polar liquids. Further investigations are desired to verify to what extent ΔG_s will be useful to characterize interactions of various coatings with variety polar solutions.

It is well known that surface topography such as pits *vs.* grooves affects differently on liquid-solid-vapor and light-solid-air interfaces. Oblate spheroids rotation and alignment under a shear field influences not only the topography but also the distribution of pigments and chemicals. This led to the characterization work in **Part B** with topography and **Part C** with coating structure influence on water soluble chemical distributions.

PART B Simultaneous Characterization of Coated Paper Topography and Optical Contrast of the Thin Layer by Near-Field Scanning Optical Microscopy (NSOM)

6. PART B, BACKGROUND AND THEORIES

6.1 Techniques for surface topography characterizations

Optical coatings are composite materials for which defining the optical properties is not a straightforward task. Coating structures are characterized by binder distribution and pigment packing such as pore and volume distributions, and particle orientations. Many techniques have been applied to studying coated paper properties. Scanning electron microscopy (SEM) has been used (McCoy 1998), which gives qualitative structural and morphological information on micro-scale. X-ray diffraction (XRD) has been used to study certain clay mineral orientations in blade coatings (Gane et al. 1995). When an entire coating layer is exposed to X-ray, due to the penetration of X-ray (Moore, Reynolds 1997), the measured orientation index is a collection of bulk coating rather than the surface property alone. Gloss goniophotometry was used to investigate pigment influence on topography and specular reflections, and results were found consistent with other studies (Gate, Leaity 1991; Hirons et al. 1998). Polarized light reflectometry was applied to studying paper coating structure, gloss and porosity (Elton, Preston 2006a,b).

The structural characterization of optical coatings is complicated by the fact that, in many cases, the spatial scale of inhomogeneities is not much smaller than the wavelength and therefore the materials scatter light significantly. In addition, these materials have appreciable roughness at the scale of the wavelength of light, which affects the scattering properties even more. As a result, macroscopical optical properties depend not only on the coating's composition but also on both the size of the particulates and the topography. Thus, it is desirable to employ characterization approaches capable of determining simultaneously the mechanical and optical properties at the surface. One such technique, near-field scanning optical microscopy (NSOM), has already been used to characterize composite materials such as 3D crystallites in Langmuir-Bludgett films of diimide and stearic acid (Dutta et al. 1999), micropatterned glass surface in liquids (Schmalenberg et al. 2002), and monolayer of silver nanoparticles (Ianoul, Bergeron 2006). In this study we report for the first time an NSOM

study of the paper coating surface morphology and its optical properties. The experimental results were obtained on high speed pilot coating trials of six formulations with mixtures of narrow and broad particle size distribution calcium carbonates and fine platy kaolin.

6.2 Surface topography and optical contrast

The surface topography of inhomogeneous media can be characterized by its roughness exponent representing the surface fractality (irregular curves or shapes), the lateral correlation length, and the interface width or root mean square (*rms*). As such, a surface can be described by the height-height correlation function, *H(r)* (Zhao et al. 1996; Hudspeth et al. 2002) that is directly related to interface width *w* and the autocorrelation function *C(r)* by $H(r) = 2w^2\left[1 - C(r)\right]$. The autocorrelation is calculated by analyzing the similarities between a series and a lagged version of itself. The correlation coefficient at lag *r* of a series $x_0, x_1, x_2, \ldots x_{N-1}$ is normally written as

$$C(r) = \frac{\sum_{i=0}^{N-1}(x_i - mx)(x_{i+k} - mx)}{\sum_{i=0}^{N-1}(x_i - mx)^2}, \qquad [6\text{-}1]$$

where *mx* is the mean of the series. For the 2D autocorrelation lengths reported in this study, the values corresponding to the 1/*e* full width of the horizontal and vertical shifts were calculated.

Light becomes diffusive when it interacts with inhomogeneous media such as optical coatings; this happens because the material composition and, hence dielectric properties vary strongly with position. In this situation imaging individual portions of the composite materials fails to provide robust quantitative information about its structure. Due to the random nature of both the material composition and the interaction of light with it, useful information can only be obtained through a statistical approach. The result of such analysis is expressed by measures like mean scattered intensity, intensity variance, optical contrast, etc.

For instance, a simple model can be developed by considering that due to inhomogeneities in the optical properties, the light is first coupled inside the medium over a volume which depends on the incident intensity. Within this volume, *N* independent elementary scattering centers are being excited, which then determine the radiation emitted from the medium. When light interacts with a limited number of individual scattering centers,

the optical contrast depends on both the number of "equivalent scattering centers" N, and the phase distribution of scattering centers, $\Delta\theta$ (Apostol et al. 2006).

$$C(N,\Delta\theta)=\sqrt{\frac{8((N-1)(N-1+\cosh(\Delta\theta^2))\sinh^2(\Delta\theta^2/2)}{N(N-1+\exp(\Delta\theta^2))^2}}\,. \qquad [6\text{-}2]$$

Thus, we use *rms* roughness, its directional correlation lengths, and the optical contrast of an NSOM image to characterize the surface morphology and local variation of optical properties.

6.3 Brief description of Near-field scattering optical microscopy

To study the effects of particle distributions on a local scale, it is necessary to probe volumes of the order, or smaller than the smallest particle inclusions. A near-field scanning optical microscope having about 50 nm spatial resolution was used which allows for the simultaneous acquisition of both local topographical and optical measurements (Paesler et al. 1996**;** Dunn 1999**)**. In reflection based NSOM (*Fig. 6-1*), light emitted from a sub-wavelength aperture fiber probe interacts with the sample, and is then recollected in the far-field (Lewis et al. 1984). The fiber couples both propagating and evanescent waves onto samples, and during the scattering process, some of the evanescent components are converted into homogeneous waves, which are then detected in the far-field by an avalanche photodiode. This conversion of evanescent to homogenous waves allows for the detection of optical effects well below the diffraction limit (Synge 1928). In order to couple evanescent fields onto the sample, the probe must be placed very near to the sample (1/50 wavelength), which can be accomplished by making use of conventional atomic force microscopy (AFM) techniques. During a near field scan, the tip is maintained at a constant separation from the sample by using a shear force feedback mechanism. Keeping this constant separation allows for the AFM topographical mapping of the sample (Lieberman et al. 1996**)**. Thus, for each location of the probe, the local topographical variation and optical signal are recorded. The magnitude of the recorded optical signal depends not only on the local values of the dielectric constant but also on the state of the physical interface. Some work has been done in attempting to decouple the mechanical and optical influences of this signal (Dogariu, Carter 2006). The aim of this report is to statistically compare samples of similar composition.

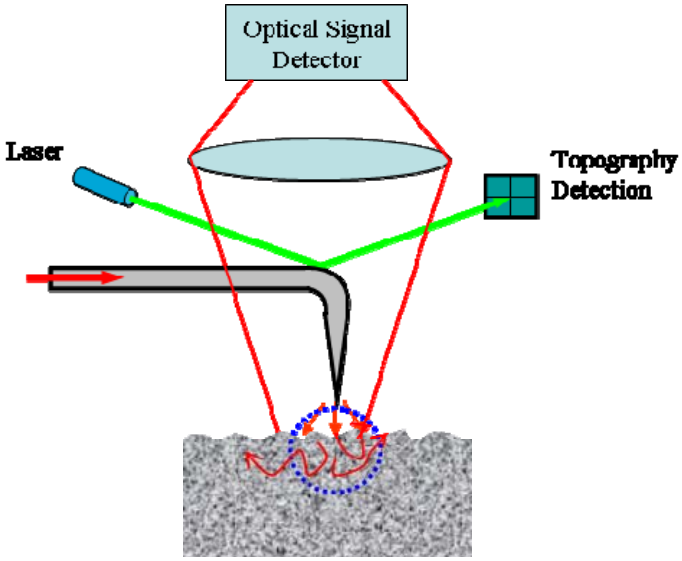

Figure 6-1 Schematic of reflection based near field scanning optical microscopy (NSOM). Light coupled to an optical fiber is emitted from a tapered fiber tip with sub-wavelength dimensions in the near field of the sample. The tip is placed and kept in the proximity (10-20 nm) of the sample using shear force feedback as common in atomic force microscopy (AFM). The probe is raster-scanned across the surface at a constant height while recording in each point an optical signal resulting from the near field scattering event as well as the topography from the AFM scan.

7. PART B, PILOT COATER RUN AND NSOM MEASUMENTES

Coatings with different combinations of pigments, designed to represent a range of coating compositions with variable porosities, were prepared as listed in *Tables 3-1,-2 and -3*, and details are listed elsewhere (Paper I). All paper rolls were supercalendered with 11 nips. A low surface roughness reduces mechanical topographic variations on NSOM. *Fig. 7-1* shows the surfaces of SEM.

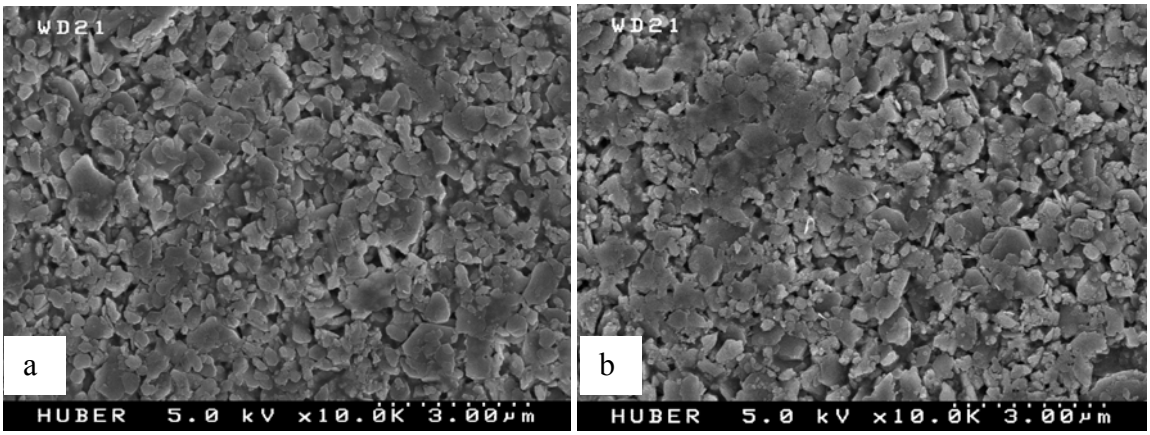

Figure 7-1 The coated and calendered paper surface under SEM (Hitachi, S-4500). (a) from sample B with 20 parts of fine kaolin having relatively closed surface structure, and (b) from sample E with 20 parts of fine kaolin.

To probe the local topographical and optical characteristics of different materials, a sample of each coating was scanned with an NSOM (Nanonics, NSOM -100). In order to compare orientation effects, all samples were aligned such that they had the same orientation with respect to the raster scanning near-field probe. To compare similar resolution in terms of both the optical and topographical images, the probe was kept at the same constant height above the different sample surfaces. Statistical information was provided by a large number of measurements; each sample was scanned three times in different locations over a square 5 by 5 μm, taking 256 by 256 measurements. Because NSOM is an interaction microscopy, the coupling between the tip and different samples may be different and could influence the average intensity scattered from different materials. However, this statistical analysis of the light-material interaction eliminates the effect of the absolute intensity, justifying the differences observed between the samples examined. The system was completely isolated for each series of scans on the individual samples, keeping the excitation power constant.

8. PART B, RESULTS AND DISCUSSION

8.1 Surface topography and optical contrast

The NSOM scan provides two images simultaneously: a topographical map and an image of local optical reflectivity. This is illustrated in *Fig. 8-1* where both images were recorded over an area of 25 square microns. There is no evident correlation between the topography and the local reflectivity. This is expected from the highly inhomogeneous nature of these materials; the local reflectivity dependence on both roughness and fluctuation of dielectric function. It is emphasized here that it is these fluctuations of the optical intensity in the near- field (*Fig. 8-1b*) that determines the far-field properties of scattered radiation.

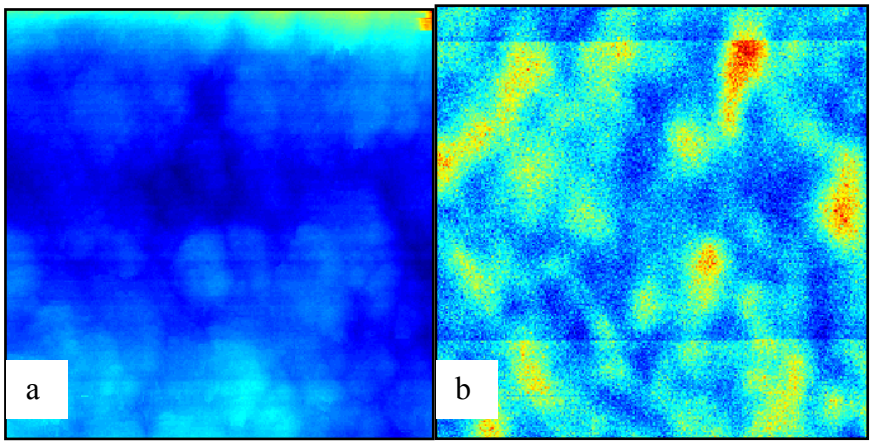

Figure 8-1(a) topography of Sample C; (b) intensity distribution from the same area of Sample C. Both image sizes are 5 by 5 μm. Note that there is no correlation between the location of high intensity points and topography features.

To provide a better assessment of the combined information, the overlaid images of light intensity (color coded with blue being the lowest intensity) on 3D topography maps are shown in *Fig. 8-2*. This representation of the NSOM results clearly revealed the differences in the optical properties as influenced by both topography and refractive index variations. Quantitative evaluations of both optical and mechanical properties will be presented in the following.

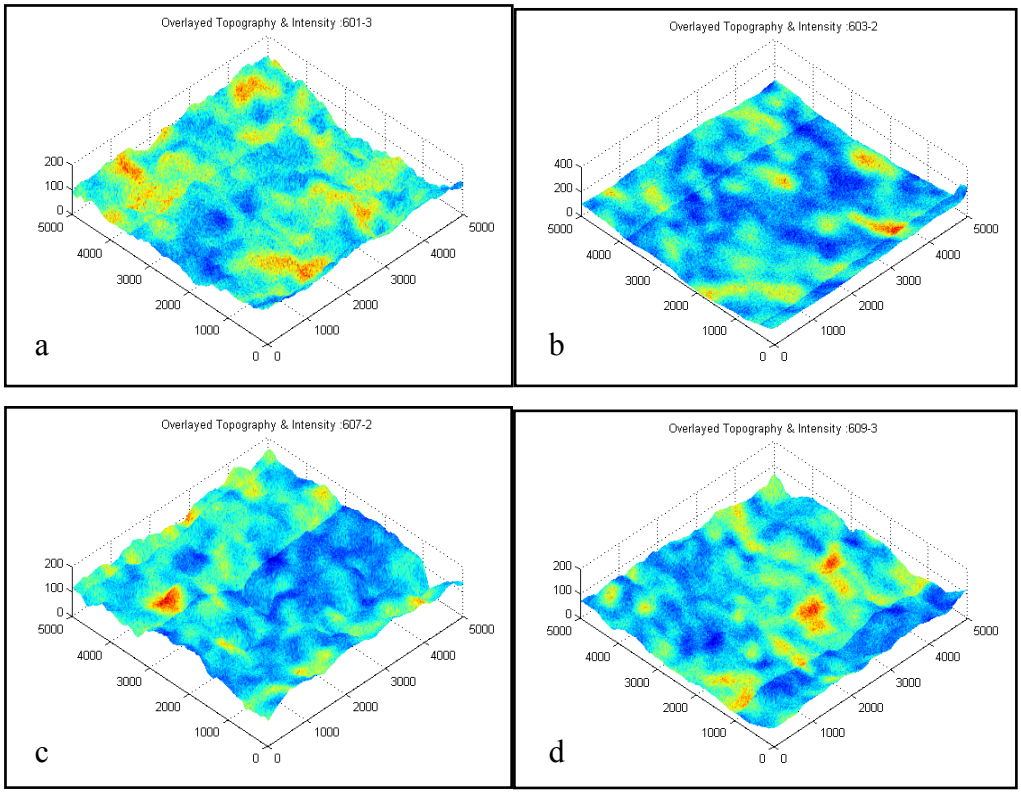

Figure 8-2 Overlaid images of the light intensity (lowest intensity denoted by blue color) and the 3D topography (height in nm as indicated). (a), (b), (c), and (d) correspond to samples A, C, D and F, respectively.

The AFM images obtained when using conventional NSOM techniques are the results of samples to tapered fiber probe force variation. The tapered fiber probe used in the experiment had a working aperture of 50nm with an approximately 150nm thick gold coating. Note that, compared to conventional diamond tip of AFM probe, the NSOM tip has in general a relatively low resolution. Therefore, an AFM (Asylum, MFP-3D) was used to verify the surface topography (*Table 8-2*). Aside from the Sample A, all the samples from AFM had the similar order *rms* (35±20 nm) as recovered from the NSOM scan. The NSOM probe was kept in a non-contact mode of operation eliminating the possibilities of cross contamination that could happen to a contact AFM measurement. The second topography measurements confirmed the accuracy of the NSOM results, allowing for further analysis of topographies and correlated optical measurements.

NSOM as a nondestructive examination tool can correlate physical and optical properties of a film to its morphology and scattering center distribution. A quick light scattering technique in far-field in place of NSOM had been considered for the measurement and calculation of $H(\mathbf{r})$ with Chandley's approach for this study. However such a calculation

has its limits because the Kirchoff approximation on which the calculation is based requires that the correlation length is much larger than the wavelength, and the local curvature of the surface is small (Nieto-Verperinas 1991). The correlation lengths (*Table 8-2*) of samples studied were in the same order as the visual wavelength, and cannot satisfy the criterion of the Kirchoff approximation. Therefore, NSOM with an AFM feature suited better for the topography characterization of smooth surface. The incapability of a far-field technique can also be practically seen from insignificant TAPPI gloss differences between the machine (MD) and cross machine (CD) directions (*Table 8-2*).

Table 8-2 Six coated samples measured with NSOM including correlation length and ratio of *x/y*, roughness and contrast. Results other than from NSOM are noted with AFM, PPs-10 (TAPPI Standard T555) and TAPPI 75° gloss (T480) in Paper IV.

	A	B	C	D	E	F
Fine kaolin	0	20	40	0	20	40
Broad GCC	100	80	60			
Narrow GCC				100	80	60
Corr. Length (*x*), µm	0.84	1.11	2.63	0.89	0.87	1.19
Corr. Length (*y*), µm	0.57	0.65	0.91	0.84	0.55	0.53
Corr. Ratio, *x/y*	1.38	1.70	2.48	1.06	1.53	1.96
Roughness rms, nm	38.4	40.6	34.1	27.7	17.1	20.8
Roughness rms, nm, AFM	97.4	54.7	39.8	53.3	27.4	45.2
Smoothness, nm, PPs-10	760	640	620	590	600	600
Optical contrast	0.199	0.204	0.199	0.183	0.177	0.188
TAPPI 75° gloss (MD)	66.5	72.8	79.4	73.7	78	80.4
TAPPI 75° gloss (CD)	66.3	73.4	80.0	74.4	77.2	80.6

In addition, the far-field TAPPI paper gloss is a specular reflection, featuring a collection of mechanical and optical surface properties. PPs is based on air leakage. The surface roughness is deducted from air leakage though it covers much larger area. In this study, the PPs weakness (with kind of *rms*) in predicting gloss except for Samples A and B can be seen from *Table 8-2*. As mentioned in the Introduction, NSOM gives both mechanical and optical descriptions simultaneously (AFM gives mechanical ones).

8.2 Coating surface roughness, correlation length and autocorrelation

The root mean square, *rms* surface roughness was calculated from the AFM topography image. A higher *rms* value corresponds to a rougher surface. Roughness fluctuations of surface height ranged from λ/10 to λ/20. As can be seen in *Fig. 8-3*, when comparing the two groups of samples one can see that the broad GCC group (A. B. and C) had an overall rougher surface than the narrow GCC group (D, E and F). This resulted in lower specular gloss level in the far-field, *i.e.* the higher *rms* the lower the TAPPI gloss as expected. Within the broad GCC and narrow GCC groups, the *rms* variations were relatively small, and no clear trend could be discerned while the correlation lengths were quite different (to be discussed in *Fig. 8-5*). This result demonstrates that roughness alone at different levels of fine kaolin within a carbonate system could not correlate to the differences seen in the specular gloss (*Table 8- 2*).

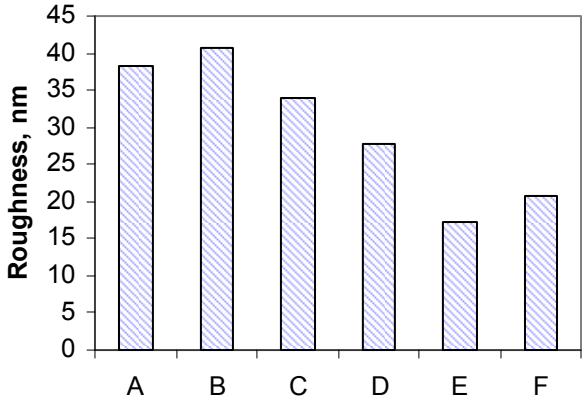

Figure 8-3 Topography roughness, root mean square *rms* in nm measured by NSOM. Broad GCC blends produced higher roughness than narrow GCC mix (Paper IV).

To quantify possible anisotropic effects, the surface correlation lengths were analyzed along different directions. The typical topography autocorrelations in *x* and *y* directions are illustrated in *Fig. 8-4*. A high autocorrelation is likely to indicate a periodicity in the signal of the corresponding time duration. For a typical anisotropic surface, the autocorrelation should be low. The results show that the sample A with no fine platy kaolin exhibits the lowest degree of periodicity. Sample B (20 parts of kaolin) on the other hand is clearly periodical in terms of its topographical features and the sample C with 40 parts kaolin is even more periodical. Similar trends are for samples D, E and F of narrow GCC. Spatial autocorrelations indicate that more fine platy kaolin tended to induce periodicities in the surface topography.

The NSOM is a raster scan. A standard with certain anisotropy is needed to calibrate the NSOM and link *x* to the direction of manufacturing. An approach to prepare such a standard has been developed. Future report is in due course.

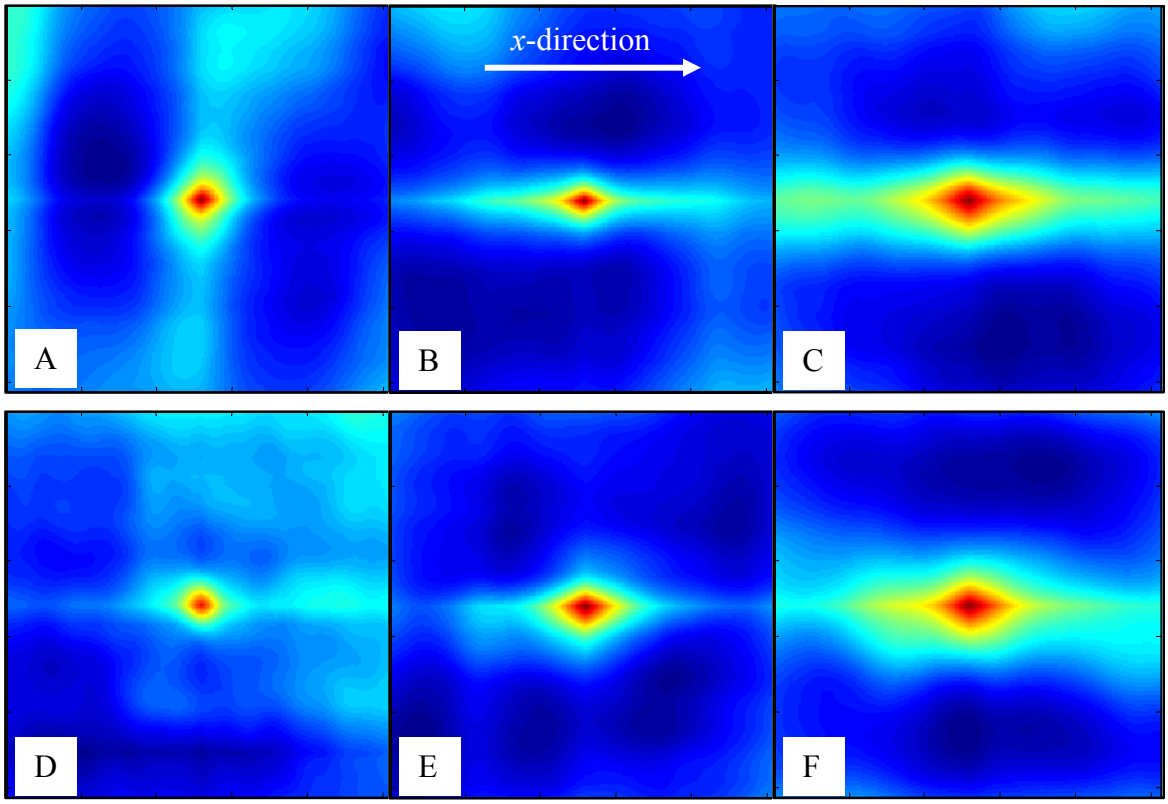

Figure 8-4 Spatial autocorrelation of topography for the six samples examined. Circular feature in the center denotes isotropy while the elongation in *x* direction indicates a periodicity in the *x* direction. The degree of periodicity accentuates when the amount of fine kaolin level increases from 0, 20, and to 40 parts in broad GCC (A), (B) and (C) and in narrow GCC (D), (E) and (F), respectively. All image sizes are 5 by 5 μm.

The quantitative correlation length ratio results are plotted in *Fig. 8-5* and, as can be seen, an interesting trend emerges as a function of kaolin concentration. Within broad GCC group, when fine kaolin level was increased, the *x/y* ratio of correlation length also increased. The same trend held true for fine kaolin added to narrow GCC. Another interesting observation is that the addition of fine kaolin to broad GCC generated higher *x/y* ratio of correlation length than to narrow GCC. While this topography in principle is expected to affect surface wetting, further study is needed to find out to what extend it would be.

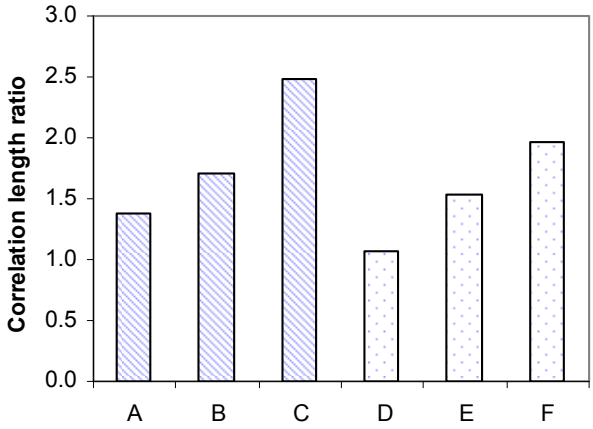

Figure 8-5 Topography correlation length ratio as measured by NSOM. Broad GCC (A, B and C) mix with fine kaolin produced higher ratio than narrow GCC (D, E and F) mix. Adding more fine kaolin increased the correlation length ratio in both calcium carbonates (Paper IV).

The fact that the addition of fine kaolin increased the correlation length *x/y* ratio can be understood as such that varying surface extends longer in *x* than in *y* direction. The higher value of correlation length in the *x* direction when the fine kaolin level was increased means that kaolin addition leads to a smoother varying surface contour in that direction. Fine kaolin particle size and shape distribution, particle rotation and alignment under shear field within a blade boundary in blade coating (Romagnoli, Bousfield 1999), compression and horizontal movement in calendering may well affect the correlation length and autocorrelations. A reduced platy particle alignment corresponding to a lower gloss gain was noted in a clay orientation study with SEM, X-ray, laser profilometry and gloss measurement (Rissa et al. 2000). It was demonstrated that facet orientation correlates better with gloss than *rms* (Chinga et al. 2003). Because of the tip convolution of non-contact feature, NSOM topography image (*Fig. 8-1*) was more diffuse than SEM (*Fig. 7-1*) and AFM (not shown). Visual evaluations with NSOM, SEM or AFM could not distinguish coated surface anisotropy. This was previously noted in using AFM to identify anisotropy within obliquely deposited gold films where quantitative analysis of the contour length was needed (Skaife et al. 2001). Further efforts are needed to study *rms* roughness, correlation length, and autocorrelation in any desired direction.

The results that broad GCC had a higher *rms* roughness than narrow GCC can be explained by several factors. Broad GCC had a higher number of coarse particles (*Table 8-1*). The large particles on the surface can increase the surface *rms* and decrease TAPPI gloss (*Fig.* 8-1).

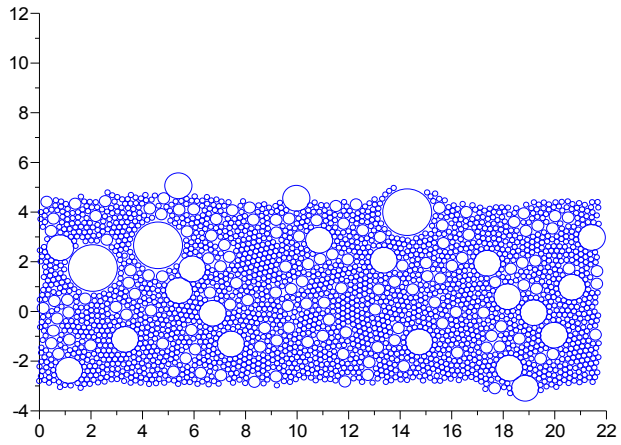

Figure 8-1 Coating layer formed after absorption flow (Paper VII).

Though the large particles can be pushed into the coating by small particles under a shear field in coating and a compression mode in calendering (*Fig.* 8-2 and 3), its disruption effect on surface network still exists to increase *rms* and reduce gloss as evident from a computer simulation and pilot trial (Paper VII).

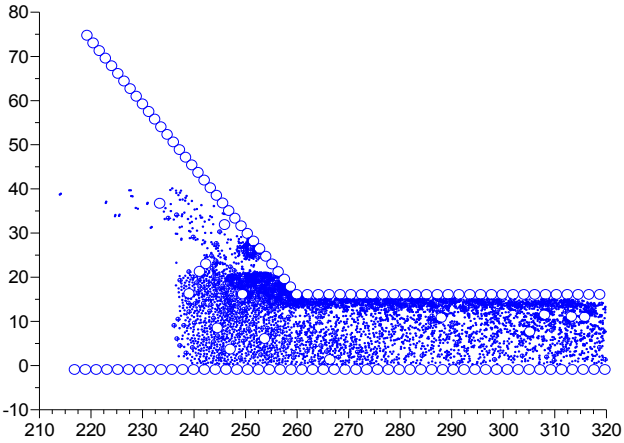

Figure 8-2 Example of blade flow simulation using five particle sizes is reported here, but no limit exists in principle on the number of particle sizes Smaller particles concentrate more towards the surface (Paper VII).

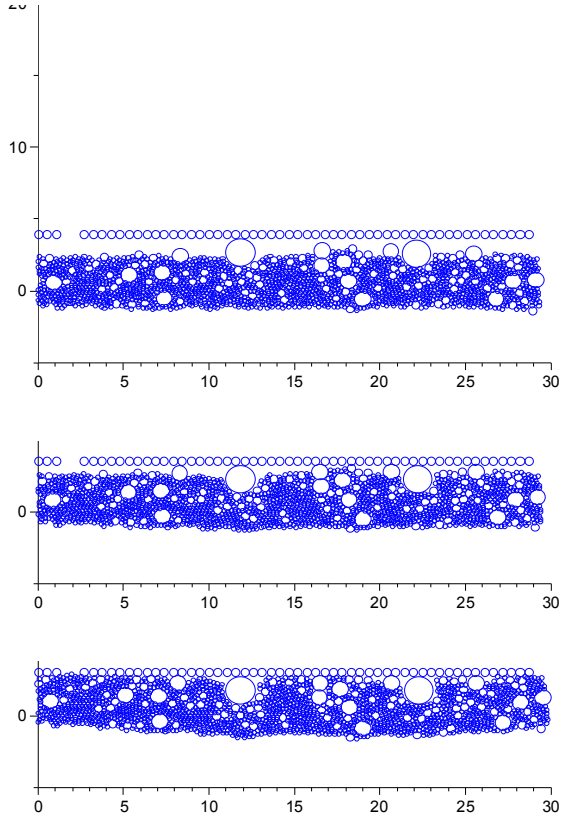

Figure 8-3 Structure being pressed by a row of particle representing the calender surface (Paper VII).

8.3 Coating surface optical contrast and scattering

The optical contrast was evaluated from the NSOM reflection images using the procedure outlined by Apostol et al. (2006). When the aperture tip scans across the surface of a sample, the coupling of radiation onto the medium is a complex process such that the magnitude of the reemitted radiation varies from point to point (*Fig. 6-1*). Histograms of the fluctuating intensity were recorded and moments of intensity distribution were subsequently calculated (*Table 8-2*). It is interesting to note that in general the optical contrast of the broad GCC group was higher than the narrow GCC group. In the mean time, the contrast evaluated within the same carbonate group did not vary significantly with the addition of fine kaolin.

The lower roughness and optical contrast of narrow GCC mix contributed to less scattered light on surface, which resulted in higher values of the specular reflectance (TAPPI 75°gloss). Broad GCC generated higher optical contrast. This can be interpreted as a combination of the increases of scattering centers and additional phases. An increase in the number of scattering centers (N) is caused by more particles in broad GCC for the same mass (*Table 3-1* and Paper VII). The additional phases ($\Delta\theta$), which had Gaussian distribution with

a width determined by the distribution of the surface heights, *rms* (*i.e.* the higher *rms* the larger $\Delta\theta$, see NSOM smoothness pair-comparisons of A *vs.* D, B *vs.* E and C *vs.* F, *Table 9-2*) led eventually to a broader distribution of phase and consequently to a higher contrast value (Apostol et al. 2006).

The rough surface of broad GCC coated paper generated low specular reflectance. However, this surface phenomenon alone does not determine the whole coating layer optical attenuation due to scattering, which is affected by an average coefficient $\alpha_{scatt} = \sigma_s \rho_V$ proportional to both scattering cross-section σ_s and the volume density of pores ρ_v. Indeed, corresponding to the same pore size distribution the broad GCC coated samples had lower pore volume density than the narrow GCC regardless of the kaolin level, as measured by mercury porosimetry (Paper IV). While this study focuses on using NSOM to characterize topographical and optical surfaces containing GCCs and fine kaolin, the surface characterized can be used in future coating studies. Zhang and Sundararajan (2007) noted that centerline average and *rms* have an effect on optical loss in the waveguide, adhesion, and friction, and autocorrelation has been used to model the adhesion of thin films etc.

9. PART B, CONCLUSION

This study demonstrates that Near-field scanning microscopy (NSOM) can be used to simultaneously characterize topographic roughness, correlation length, autocorrelation, and optical contrast from the same area of coated paper surfaces. The optical contrast of light field in the proximity of the coating layer is an indication of sample diffusivity. While the process of light scattering is complicated by the influence of both topography and variation of refractive index, the experiments clearly indicate that coatings characterized by higher gloss manifest lower values of the near field optical contrast. Moreover, they suggest that both surface roughness and correlation length affect the physical and optical properties.

It also observed that the addition of fine kaolin increased the topography correlation length resulting in a smoother varying surface contour. Furthermore, the topography correlation length increased with different amounts in orthogonal directions indicating the creation of a certain degree of surface anisotropy. This feature was calculated for both sets of samples examined, broad and narrow distribution GCCs even though the narrow GCC combination with fine kaolin produced, in general, a lower topography roughness and optical contrast which can be translated into higher specular reflectance (TAPPI 75° gloss).

PART C The influence of fine kaolin and ground calcium carbonates on the efficiency and distribution of fluorescence whitening agents (FWA) in paper coating

10. PART C, BACKGROUND AND THEORIES

Fluorescence whitening agents (FWA) are widely used in paper to increase whiteness. It is well known that a base paper containing wood fiber absorbs UV light and reduces the efficiency of FWA (Johnson 1991; Johansson 2000; *e.g.* Forsskåhl 2000). In paper coating, other factors are more critical as evidenced from a distyrylbiphenyl (DSBP) FWA lab study in the correlation of absorption and fluorescence, the yield between absorbed and emitted light, and the position of saturation point (Rohringer, Fletcher 1996). In a lab study of pre-moisturized pre-coat to prevent top-coat FWA from migrating into pre-coat, it was proposed to use FWA in top-coat and TiO_2 in pre-coat (Heikkilä et al. 1998). In a recent study of coating over glass, the reflectance was found to range between 60-80%, and for kaolin it was somewhat higher in the visible region but lower in the UV-region (Fjellström et al. 2007a). The previous studies featuring lab-scale used kaolin and calcium carbonate separately without investigating the coating structure of fine kaolin and carbonates blend impacts on optical properties.

The FWAs used in paper industry are mainly sodium-salts, thus water soluble. The π-electrons in the conjugated chain absorb ultraviolet radiant energy in 300-360 nm wavelength and re-emit the energy mainly in 400-450 nm, blue light range. FWA distribution is affected by paper and coating chemistry, coating and drying process. A pilot scale coating is a proper way to simulate the complicated coating process. We conducted a pair-comparison pilot coating, then a pilot-scale design of experiment (DOE) to investigate kaolin and calcium carbonate, and coating structure effects on FWA efficiency.

In an effort to describe the optical properties of highly scattering materials while reducing the computational difficulties, simplifying flux models have been designed for the radiative energy transport. A volume scattering medium consisting of a collection of scattering centers is described as homogeneous material characterized by effective scattering and absorption properties that are determined by its internal structure. In this approach, the fundamental equation of radiative transfer is based on the balance between the net flux

change, the flux input, and flux continuing out in an infinitesimal volume. Assuming two diffusing components, a one-dimensional model based on plane symmetry for unit cross section was initially proposed (Schuster 1905). The model relates the phenomenological, effective scattering $S_{K\text{-}M}$ and absorption $K_{K\text{-}M}$ coefficients to measurable optical properties such as diffuse reflectance or transmittance. The most successful extension of this model is the so-called Kubelka-Munk (KM) theory (Kubelka, Munk 1931).

A considerable body of work was dedicated to relate the KM parameters to microstructure and to incorporate both the single- and multiple-scattering effects. Refinements and higher order flux models were developed. A more accurate model that accounted for the usual condition of collimated incident radiation was elaborated (Reichman 1973). A four-flux model was developed that includes certain anisotropy of the scattered radiation (Maheu 1984). A six-flux model was implemented to incorporate the effect of particle shape and inter-particle correlation (Emslie 1973). In spite of the fact that it is based on empirical determination of coefficients and that its range of applicability is rather unclear, the simple-to-implement KM theory gives a reasonably good description of experiments and has found applications in areas such as coatings, paper, paints, pigments, medical physics, and atmospheric physics.

Initially the internal reflection of photons at the medium's boundaries was ignored. Later, the reflectance was included to show that by theory and experiment, the reflectance and absorption of a non-homogeneous specimen depend on the direction of illumination, whereas transmittance does not (Kubelka 1948, 1954). In addition to the assumptions mentioned already, the difficulties in using KM equation in this multi-layer coating study are that it does not have a wavelength parameter, the scattering coefficients of different layers cannot be experimentally determined from a coated whole sheet, and the scattering coefficients vary as thickness changes.

Assuming the normal incidence of a beam with irradiance $\boldsymbol{I_i}$ (*Fig. 10-1*), the total flux transmitted through a slab is given by (Bohren, Huffman 1998)

$$I_t = I_i(1-R)^2 e^{-\sigma h}(1+R^2 e^{-2\sigma h} + R^4 e^{-4\sigma h} + \ldots), \qquad [10\text{-}1]$$

where h denotes the thickness of the slab, the optical absorption coefficient $\alpha = \frac{4\pi k_1}{\lambda}$, λ denotes the incident wavelength, and k_1 denotes the imaginary part of the complex refractive index of the material. The reflection coefficient R of an optically smooth surface is

$$R = \frac{(n_1 - 1)^2 + k_1^2}{(n_1 + 1)^2 + k_1^2}, \qquad [10\text{-}1\text{-}1]$$

where n_1 is the real part of complex refractive indexes of the slab.

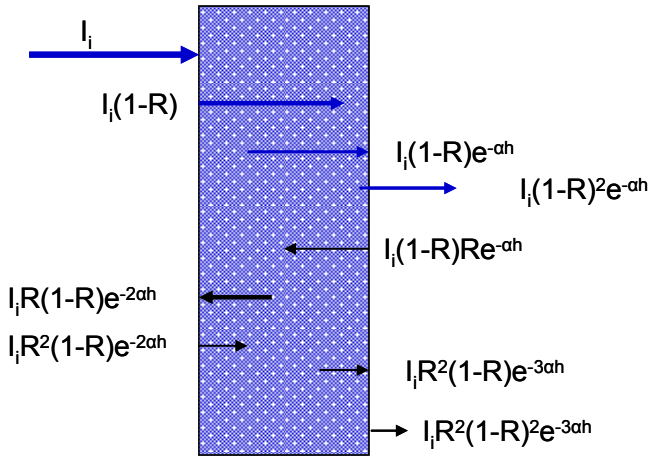

Figure 10-1 Transmission of a slab, only the first two components of *Eq. [10-1]* contributing to the total are shown (Bohren, Huffman 1998).

It is interesting to note that a heuristic criterion for smoothness is $d < \lambda/8$ where d is the height of surface irregularities (Beckmann, Spizzichino 1963). Glossy coated paper with fine kaolin and calcium carbonate has a typical roughness, σ_h = 15-40 nm as measured by near-field scanning optical microscopy (NSOM) (Dogariu, Carter 2006) and, therefore, satisfies this smoothness criterion.

The total transmittance through the slab is obtained by summing up the infinite series in *Eq. [10-1]* to find

$$T_{slab} = \frac{(1-R)^2 e^{-\alpha h}}{1 - R^2 e^{-2\alpha h}}. \qquad [10\text{-}2]$$

A further approximation can be used to simplify *Eq. [10-2]*. If the secondary reflection from the other side of the slab $R^2 e^{-2\alpha h}$ is small compared with unity, which is

basically true for light transmittance in a very opaque pigment coating, then *Eq. [10-2]* reduces to

$$T_{slab} = (1-R)^2 e^{-\alpha h} \qquad [10\text{-}3]$$

Though it includes the wavelength parameter, there are a number of practical aspects which are not accounted for in this representation. First, the coating layer has many small air voids of refractive index around unity (LePoutre 1989), which significantly increases the importance of scattering in comparison with absorption. Another complication arises in paper coatings that have random multi-particle orientation and packing, *i.e.* variety of optical dipoles with distributions from multi-ingredients, irregular air void size and shape distributions on both the surface and the inner layer of a coating. Moreover, optical interfaces are not homogeneous as assumed in this approximation. Due to variations in surface topography and dielectric properties along the interface, a confinement of evanescent waves occurs in the near-field of media random coating layer that may affect statistical properties of optical fields in the vicinity of interfaces (Apostol et al. 2006). More advanced optical scattering theories, such as T-matrix and coupled (discrete) dipoles approximation (CDA) *etc*. may be utilized to describe the scattering from inhomogeneous coating layers (Tsang et al. 2001).

For the purpose of this discussion about coating pigment and structure influence on FWA efficiency within a porous paper coating, we treat the coating layer as a unit and use the extinction coefficient of a coating layer in an approximate equation in the form of

$$T_{coating} = (1-R)^2 e^{-\alpha_{EXT} h} \qquad [10\text{-}4]$$

where the α_{EXT} denotes extinction coefficient

$$\alpha_{EXT} = \alpha_{scatt} + \alpha_{abs} = \sigma_s(\lambda)\rho_V + \alpha_{abs} \qquad [10\text{-}5]$$

Eqs. [10 -4, -5] imply that as far as absorption is concerned high reflectance and thickness, as well as low wavelength reduces the light transmittance, $T_{coating}$. In porous paper coating, the attenuation due to absorption, α_{abs} remains relatively the same because it is primarily determined by the chemical composition and molecule structure of the coating

chemicals *i.e.* both broad and narrow GCCs are calcite calcium carbonates. The attenuation due to scattering is measured by an averaged coefficient $\alpha_{scatt} = \sigma_s \rho_V$ that is proportional to both scattering cross-section σ_s and the volume density of pores ρ_v. Hence, the scattering coefficient is directly affected by the increase in pore volume fraction. As a result, the attenuation increases significantly due to the increase of σ_s and ρ_v. We note that $\alpha_{scatt} = \sigma_s(\lambda)\rho_V$ varies depending on wavelength, and is valid for a mono sized pore distribution, but in real coating one has an entire distribution of sizes. However, this would only make the result more specific to a particular coating composition, but will not affect the main conclusion that the increase in pore size of given wavelength and number leads to an increase in scattering. Also, it will not affect the statement about the wavelength dependence of attenuation that is not included in the KM approximation. Another important observation relates to the wavelength dependence of the scattering cross section of an air pore. This is the origin of the spectral variations in both transmission and reflection from diffusing coatings.

11. PART C, EXPERIMENTAL

11.1 Pigment properties of coatings

The first coating trial was run with paired-comparisons (*Table 11-1*). The second, a 3-factor DOE (the same pigments with different levels while all the other factors were the same as in the first trial), totaling eight trial points, was a mixture design and optimized with distance-based optimality. The DOE design and analysis was done with Minitab 15 statistics software (Minitab, USA). Ground calcium carbonates, with broad size distribution at 95.3 TAPPI brightness and 0.42 b-value; with narrow size distribution 94.9 TAPPI brightness and 0.26 b-value were from Omya AG. The fine kaolin at 90.9 TAPPI brightness and 2.19 b-value was from KaMin LLC. The TAPPI brightness and b-value by TAPPI T452 (Technidyne) were measured at KaMin LLC, Macon, Georgia, USA (*Table 3-1*). Wood free base paper was from Fraser Papers, Canada: basis weight 62 g m^{-2}; TAPPI brightness 85.4 and b-value 4.1.

11.2 Preparation and properties of coatings

Coatings with different combinations of pigments, designed to represent a range of coating compositions with variable porosities (*Table 11-1*) were prepared on pilot scale according to the pilot coating facility procedures in Part A (Paper I and II). The coatings were applied on a wood free base paper using a pilot coater in Trois-Rivières, PQ, Canada, and details are listed elsewhere (Paper I).

Table 11-1 Pigment compositions of first pilot coating, in parts by weight. In addition, all other coating chemicals were the same as in Paper I.

Topcoat	**A**	**B**	**C**	**D**	**E**	**F**
Fine kaolin	40	20		40	20	
Broad GCC	60	80	100			
Narrow GCC				60	80	100
Solids of coating, %	65.2	65.7	65.0	65.0	65.0	65.2
WRV, g/m^2	119	134	153	164	183	211

11.3 Optical measurements of coated samples

The coated paper samples were prepared and conditioned according to TAPPI standard T402. TAPPI brightness was determined with 457 nm wavelength light (light source A standard, *Fig. 11-2*) by TAPPI T452. ISO CIE whiteness was measured with diffused light source (light source D_{65}/10° standard with more UV than TAPPI brightness standard) according to ISO 11475:2000. Whiteness is defined as the reflectance of light across the visible spectrum including color components in the measurement. Brightness is defined as the reflectance of light at the wavelength of 457 nm without color in the measurement. Due to this difference, whiteness becomes important in paper industry (*e.g.* Lekelä 2000).

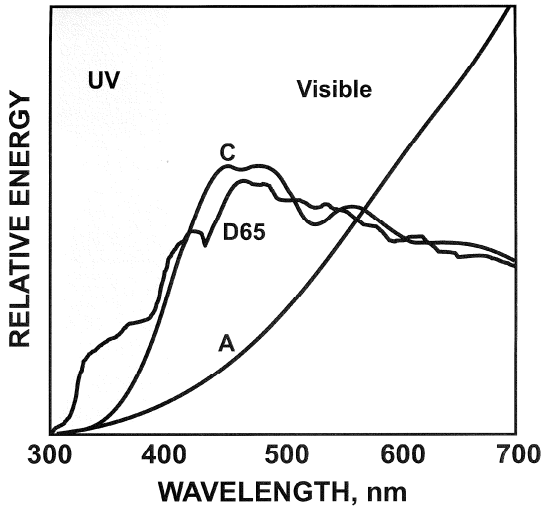

Figure 11-2 Spectral energy distributions of standard illuminates A, C, and D_{65} (*e.g.* Crawford et al. 1996).

For the analysis of FWA distribution in thickness direction, paper samples were embedded in epoxy resin. A cross section of 5 μm thickness was sliced with a dry diamond knife. A cooled digital camera was used to capture the image under Zeiss Axioplan UV-light microscope in reflective mode with a fluorescence filter. To keep constant light intensity, 20 ms exposure time was used for each sample, respectively (KCL Oy, Espoo, Finland).

12 PART C, RESULTS AND DISCUSSION

12.1 Coating structure with fine kaolin and calcium carbonate

The coating pore structures of coated paper samples were characterized with mercury intrusion (Paper I). When blended with 20 and 40 parts of fine kaolin, narrow GCC generated higher pore volume than broad GCC with the same pore diameter ranges (*Fig. 12-1*). This was also true for 100 parts of GCCs (not shown here). Based on *Eqs. [10- 4, -5]*, a larger pore volume density, ρ_V increases the light scattering coefficient, α_{scatt} and consequently reduces the light transmittance $T_{coating}$.

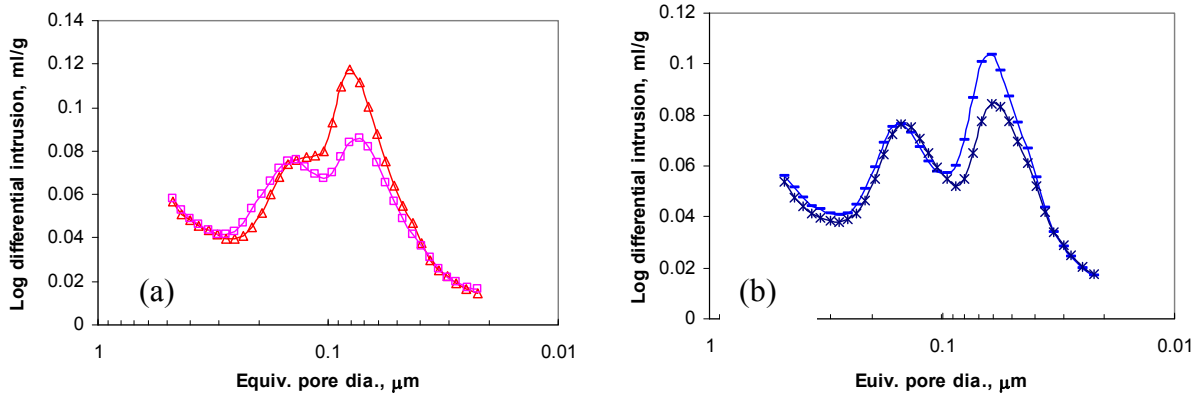

Figure 12-1 Coating pore structure in the pore diameter range of 0.02 – 0.5 µm. (a) with 20 parts of fine kaolin narrow GCC (Δ) has higher pore volume than broad GCC (□); (b) with 40 parts of fine kaolin narrow GCC (-) has higher pore volume than broad GCC (x) in Paper V.

12.2 GCC type and kaolin level influence on TAPPI brightness and CIE whiteness

As the base paper and pre-coat were kept constant, the effect of brightness difference of coated paper was more determined by the top-coat pigment brightness and packing. The increase of kaolin level led to lower brightness in blends with either broad GCC or narrow GCC (*Fig. 12-2*). The pigment brightness and b-value of broad GCC were 0.4 and 0.16 (less blue) points higher than those of narrow GCC, respectively. However, compared to broad GCC, narrow GCC generated higher coated paper brightness. This is expected from discussions on optics and coating pore structure. The coated paper brightness is increased by the high scattering power of narrow GCC coatings that can hide the dark base paper better.

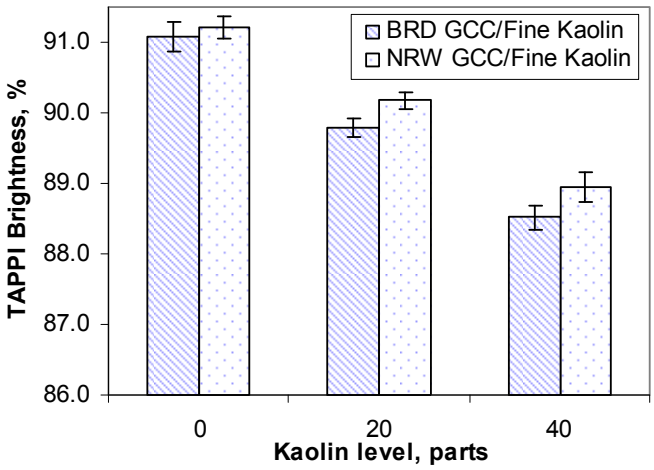

Figure 12-2 TAPPI brightness of coated paper with broad (BRD) GCC and narrow (NRW) GCC with fine kaolin level from 0 to 40 parts (Paper V).

Broad GCC generated CIE whiteness higher than or equal to that of narrow GCC across the levels studied (*Fig. 12-3*). The addition of kaolin reduced CIE whiteness regardless of GCC types. Besides the features of TAPPI reflective *vs.* ISO diffusive lights, TAPPI light source has a very low level of UV light while the CIE whiteness light source D_{65} is similar to outdoor daylight that contains higher level of UV light (*Fig. 11-2*). Coating structure has influence on light scattering. The higher scattering power of narrow distribution pigment packing affects not only the attenuation of the forward scattering but also the backscattering when the light is multi-scattered before it exits either side of coated paper. Furthermore, various particle size and shape distributions have different light scattering and absorption efficiencies (*e.g.* Bohren, Huffman 1998).

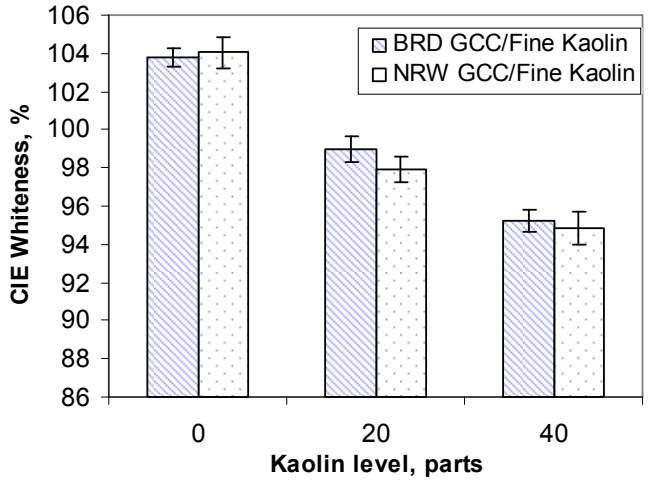

Figure 12-3 ISO CIE whiteness of light source D_{65} from broad (BRD) GCC and narrow (NRW) GCC with fine kaolin level from 0 to 40 parts (Paper V).

12.3 GCC and kaolin packing influence on CIE whiteness

The samples (*Table 12-1*) of second pilot coating trial run on a mixture DOE design were analyzed to statistically predict the coating structure influence over brightness and CIE whiteness.

Table 12-1 Analysis of Variance (ANOVA) for TAPPI brightness and CIE whiteness of coated paper samples (component proportions) with the estimated regression coefficient.

	Broad GCC	Narrow GCC	Kaolin	*p*-value	Probability of Linear coefficient
TAPPI Brightness, %	75.5	87.3	72.6	0.021	0.3
CIE Whiteness, %	133	109	108	0.006	0.07

The quadratic regression with *p*-value =0.021 shows that TAPPI brightness was affected by the pigment types and PSD with narrow GCC having the highest brightness contribution. However, the whole regression cannot be calculated linearly (*p*-value = 0.3). The regression coefficients with *p*-value = 0.006 for CIE whiteness shows the equality of narrow GCC and fine kaolin while broad GCC had the highest contribution to CIE whiteness. The probability of linear coefficient *p*-value =0.07 allows a linear regression with 90% confidence level. This DOE based trial statistically confirmed the TAPPI brightness and CIE whiteness results of the first pilot trial. Moreover, the lower regression linear coefficient pointed to the weak compatibility of high brightness narrow GCC with FWA when compared with broad GCC (109 vs. 133). The surface response (*Fig. 12-4*) shows that to have high CIE whiteness, the level of narrow GCC needs to be increased. Furthermore, the response surface of different pigment system has its uniqueness for regional optimization.

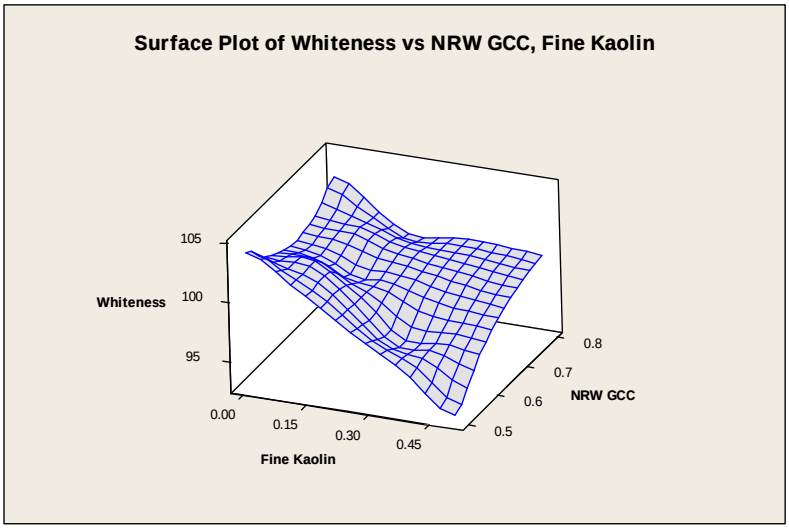

Figure 12-4 Mixture DOE of high level of narrow (NRW) GCC (0-80 parts) with fine kaolin (0-50 parts) in Paper V.

The DOE statistical prediction of this coating study reveals that for visual wavelength lights a high α_{scatt} is needed to reduce light transmittance and to cover the dark base paper. It also, however, shows that for UV light that is attenuated more in the coating (*Eq. [10-4, - 5]*), a low α_{scatt} is needed to increase UV light transmittance and to generate more blue light from FWA. An increase of α_{scatt} to UV light is due to a larger ρ_V, and to a possible $\sigma_s(\lambda)$ increase as wavelength decreases (it is also possible to have a case of $\sigma_s(\lambda)$ decrease but its magnitude must be in the range to give a net increase of $\alpha_{scatt}= \sigma_s(\lambda)\rho_V$). In either case, the combination of ρ_V and $\sigma_s(\lambda)$ makes α_{scatt} larger in narrow GCC than in broad GCC to attenuate short wavelength UV light more as reflected in low CIE whiteness, *i.e.* a reduced UV efficiency. While the $\alpha_{scatt} = \sigma_s(\lambda)\rho_V$ contribution to $T_{coating}$ in a multi-coating is discussed, a complete evaluation of *Eq. [10-4, -5]* requires that the thickness, h impact, *i.e.* FWA distribution in the thickness direction be further investigated.

12.4 FWA distribution in coatings with different kaolin levels

For all the microscopy illuminated with UV light (*Fig. 12-5*), the FWA of 100 parts of coarse GCC pre-coat mostly concentrates at the interface of pre-coat and base paper (since base paper does not have any FWA, it appears black in the image). Though the CMC level was higher in pre-coat (0.7 *vs.* 0.5 parts of top-coat), the blade pressure and capillary adsorption combined with porous coating of coarse GCC caused rather severe dewatering that brought FWA to the interface and anchored there, and left very little FWA to migrate towards surface

during drying of post pre-coating. It is interesting to note that the FWA concentration at the interface of pre-coat and top-coat is much lower than at top surface (*Fig. 12-5c*). This indicates that in this high speed coating with jet applicator and bevel blade the dewatering from top-coat into the pre-coat is much weaker than from pre-coat into base paper. For all the top coatings (the interface of top and pre-coat can be located at an even split of total coating thickness as shown in *Fig. 12-5b*). The 100 parts narrow GCC (*Fig. 12-5*a) has a rather uniform intensity of FWA in thickness direction. When 20 parts of fine kaolin (*Fig. 12-5b*) was added at the expense of narrow GCC, the FWA concentrates more toward surface, and this becomes even more evident when 40 parts fine kaolin (*Fig. 12-5c*) was added. Digital imaging analysis for the top 1/3 of coating layer thickness of the cross section produced 183, 151, 125 blue levels (it is based on 2^8 = 256 blue level, the larger number the brighter) for sample D, E, F, respectively (Adobe, Photoshop®, USA).

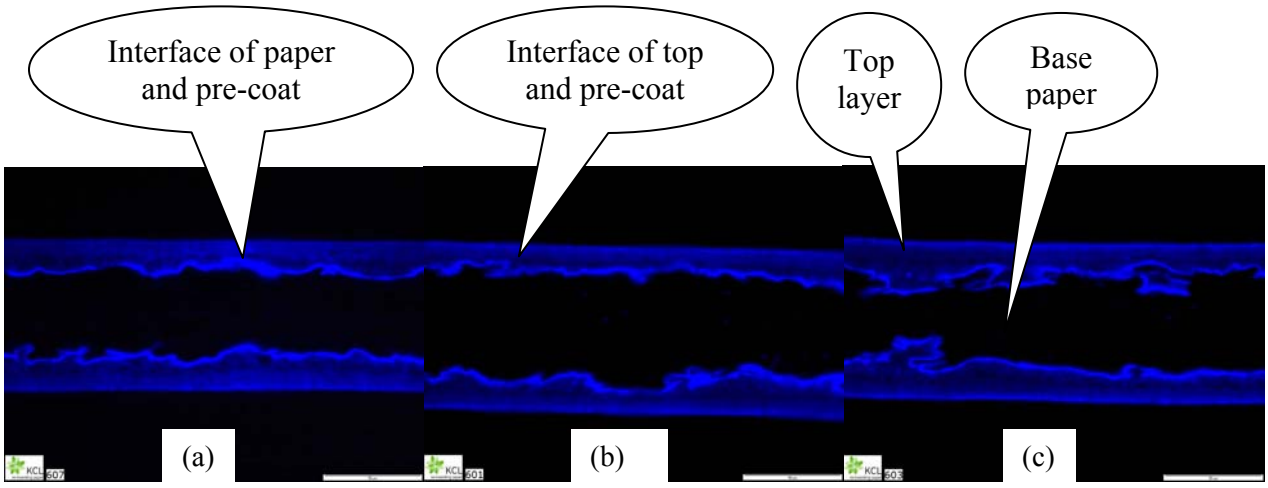

Figure 12-5 (a) has 100 parts of narrow GCC in top-coat; (b) 80 parts NWR GCC and 20 parts of fine kaolin in top-coat; and (c) 60 parts of narrow GCC and 40 parts of fine kaolin in top-coat. Coated paper cross section of microscopy illuminated with UV light. The dark middle layer is the base paper that has no FWA. FWA of pre-coat heavily concentrates at the interface of pre-coat and base paper while the FWA of top-coat concentrates more at top surface with the addition of fine kaolin at the expense of narrow GCC (Paper V).

Recalling the discussions above, *Eqs. [10 -4, -5]* and *Fig. 12-5*, one can make several observations. For high efficiency, FWA should be concentrated near the top surface because this is where the short wavelength UV light is least attenuated, and most exposed to the backscattered UV light from the coatings. The FWA of pre-coat concentrates at the interface

(approximately 20 μm of an average thickness) of pre-coat and base paper. The high α_{scatt} and h at the interface produces the less UV transmittance based on *Eq. [10- 4 and 5]*, making the FWA of pre-coat the least efficient. This note about FWA distribution can be extended to single blade and film coatings where the FWA distribution is affected by the same mechanism as pre-coat, *i.e.* through the interactions between base paper and coating. Wood free or ground wood base paper and board often contains FWA for the whiteness and uniformity from multi-scattering properties. Broad GCC with fine kaolin can further improve CIE whiteness by allowing more UV light to transmit to the pre-coat and base paper to generate more blue lights and to be backscattered through it. Kaolin has lower brightness and absorbs more UV light than carbonates (*e.g.* McComb, Stickler 1995). This study shows that this can be partially compensated by the fine kaolin ability of retaining and allowing the migration of FWA towards the surface to make FWA more efficient. If a wood free base paper has high yield pulp, kaolin containing coating layer can more effectively screen UV to reduce light-induced brightness reversion of high yield pulp (Yuan et al. 2006). This study suggests that for FWA efficiency, uniformity and UV screening it is desirable to design a carbonate and kaolin pigment system to produce a gradient FWA distribution in thickness direction with the highest FWA concentration towards the surface.

13. PART C, CONCLUSION

This study found that increasing fine kaolin level at the expense of narrow GCC made FWA concentrate more towards the surface as shown by cross sections of microscopy under UV light. Pigment coating structure affects the FWA efficiency mainly in the ways of light scattering and FWA distribution in thickness direction. The combination of pore volume density, ρ_V and scattering cross-section, $\sigma_s(\lambda)$ makes α_{scatt} larger in narrow GCC than in BRW GCC to attenuate short wavelength UV light more, *i.e.* a reduced UV efficiency. It is desirable to design a carbonate and kaolin pigment system to produce a gradient FWA distribution in thickness direction with the highest FWA concentration towards the surface. While its brightness and whiteness are lower than carbonates fine kaolin has a function to improve FWA efficiency by making FWA least attenuated in forward scattering and most exposed to the backscattered UV light near the surface.

14. CONCLUSIONS

Characterization of a coating structure by mercury intrusion may be used to calculate the total Gibbs energy (ΔG_s) of capillary imbibition for a given liquid into a heterogeneous porous coating at the final state. This novel utilization of the Gibbs energy concept combines coating structure variables (volume and diameter, $\sum(V_i/D_i)$) and surface energy parameters ($\gamma cos\theta$) at the liquid-coating-vapor interface. Furthermore it shows that the ΔG_s is a better characteristics of capillary imbibition than each parameter alone. The good match between the time needed to reach the maximum tack force (t_{max}) and the Gibbs energy on both coated paper and board applications leads to the conclusion that though many factors affect the capillary imbibition in the initial state and the rate of access to the final state, the calculation of ΔG_s appears to reflect the effect of coating structure and surface energy on the imbibition of ink until the maximum tack is reached. A larger capillary pore surface area strongly increases ink setting rate, as measured by the shortened t_{max}. Comparisons of different kaolin and latexes show that the base parameters γ^- (in the vOCG approach) are low compared to Lifshitz-van der Waals interactions, γ^{LW} while the acid γ^+ component is negligible. Moreover, using kaolin coatings with constant γ^{LW} and different γ^- changes the Gibbs energy and coated paper capillary adsorption in offset ink setting, as seen in the different t_{max}, but there is no effect on the maximum tack force, F_{max} and the final tack. However, compared to styrene/n-butyl acrylate latex, n-butyl acrylate-acrylonitrile-styrene latex that lowers γ^{LW} on coated board surface significantly increases t_{max}, and reduces F_{max} and the final tack.

In addition to introducing the Gibbs energy concept, this thesis shows that Near-field scanning microscopy (NSOM) can be used at the light-solid-air interface to characterize topography with roughness, correlation length and autocorrelation, and optical contrast from the same area of coated paper surfaces in one single measurement. The addition of oblate spheroids increases the coated paper topography correlation length resulting in a smoother varying surface. Moreover, the topography correlation length increases with different amounts in orthogonal directions indicating the creation of a certain degree of surface anisotropy. Finally, it shows by UV microscopy of cross-sections of paper that increasing fine kaolin level in coatings causes FWA to concentrate more towards the surface. The combination of pore volume density, ρ_V and scattering cross-section, $\sigma_s(\lambda)$ makes the

scattering coefficient, α_{scatt} larger in narrow GCC than in broad GCC coatings and, hence, short wavelength UV light is attenuated more, *i.e.* UV efficiency is reduced

Future basic studies will be to apply the Gibbs energy model with the topography characterized by NSOM at the liquid-solid-vapour/air interfaces of thin layer porous coatings with nano particles.

REFRENCES

1. Adamson, A. and Gast, A. *Physical Chemistry of Surfaces,* 6th Ed. John Wiley & Sons, New York, **1997**.

2. Apostol, A., Haefner, D. and Dogariu, D. *Phys. Rev.* E 74, 066603, **2006**, 1.

3. Beaglehole, D. *J. Phys. Chem.* **1989**, 93(2), 893.

4. Beckmann, P. and Spizzichino, A. *The light scattering of electromagnetic waves from rough surfaces,* Macmillan, New York, **1963**.

5. Bohren, C.F. and Huffman, D.R. *Absorption and scattering of light by small particles,* John Wiley & Sons, New York, **1998**.

6. Bosanquet, C. H. *Philos. Mag.* **1923**, S6 (45), 525.

7. Chinga, G., Gregersen, Ø. and Dougherty B. *J. Microscopy and Analysis*, **2003**, 84, 5.

8. Chinga, G. and Helle, T. *J. Pulp Paper Sci*. **2003**, 29, 179.

9. Crawford, P. M. and Crawford, T. B. *Measurement and Control of the Optical Properties of Paper,* 2nd Edition, Technidyne Corporation, New Albany, **1996.**

10. Della Volpe, C. and Siboni, S. *J. Adhesion Sci. Tech.* **2000**, 14(2) 235.

11. Derjaguin, B., Starov, V.M. and Churaev, N.V. *Colloid J.* **1976**, 38(5), 875.

12. Dogariu, A. and Carter, R.D. *9th TAPPI Advanced Coating Fundamental Symposium,* **2006**, pp323-327.

13. Donigian, D.W., Ishley, J.N. and Wise, K.J. *TAPPI Proc. Coating Conf*., **1996**, TAPPI Press, pp. 39-48.

14. Dunn, R. C. *Chem. Rev.*, **1999**, 99, 2891.

15. Dunnett, C.W. *Biometrics,* **1964,** 20, 482.

16. Dussan, E.B., Rame, E. and Garoff, S. *J. Fluid Mech.* **1991**, 230, 97.

17. Dutta, A.K., Vanoppen, P., Jeuris, K., Grim, P.C.M., Pevenage, D., Salesse, C. and De Schryver, F.C. *Langmuir,* **1999**, 15, 607.

18. Elton N.J., and Preston, J.S. *Tappi J.* **2006a**, 5(7), 8.

19. Elton N.J., and Preston, J.S. *Tappi J.* **2006b**, 5(8), 10.

20. Emslie, A. G. and Aronson, J. R. *Appl. Opt.* **1973**, 12, 2563.

21. Fisher, L.R., and Lark, P.D. *J. Colloid Interface Sci.* **1979**, 69, 486.

22. Fisher, L.R., and Israelachvili, J.N. *J. Colloid Interface Sci.* **1981**, 80(2), 528.

23. Fjellström, H., Höglund, H., Forsberg, S., Paulsson, M., and Rundlöf, M. *Nord. Pulp Paper Res. J.* **2007a**, 22(3): 343.

24. Fjellström, H., Höglund, H., Forsberg, S., Paulsson, M., and Rundlöf, M. *Nord. Pulp Paper Res. J.* **2007b,** 22(3): 350.

25. Forsskåhl, I. *"Brightness reversion", In: Forest products chemistry*, Ed. Stenius, P. Fapet Oy, Helsinki, Finland, **2000**, 278-332.

26. Franco, F. and Ruiz Cruz, M.D. *Clay Miner.* **2004**, 39, 193.

27. Gane, P.A.C., Hopper, J.J. and Grundwald, A. *TAPPI Coating Conf. Proc.* **1995**, TAPPI Press, Atlanta, pp383-390.

28. Gane, P.A.C. and Seyler, E.N. *TAPPI Coating Conf. Proc.*, **1994**, TAPPI Press, pp. 243-260.

29. Gane, P.A.C., Matthews G.P., Sechoelkopf, J., Ridgway, C.J. and Spielmann, D.C. *TAPPI Coating Fundamental Symposium,* **1999**, TAPPI Press, pp.213-236.

30. Gate, L.F. and Leaity, K. *TAPPI Coating Conf. Proc.* **1991**, TAPPI Press, Atlanta, pp473-481.

31. de Gennes, P.G. *Rev. Mod. Physi.* **1988**, 57, 827.

32. Good, R.J. *J. Adhesion Sci. Technol.* **1992**, 6(12), 1269.

33. Gu, W., Bousfield, D.W. and Tripp, C.P. *Nord. Pulp Paper Res. J.* **2007**, 22(1), 57.

34. Heikkilä, K., Alatalo, M. and Grankvist, T. *TAPPI Coating Conf. Proc.,* **1998**, TAPPI Press, pp355-372.

35. Hiorns, A.G., Elton, N.J., Coffon, L. and Parsons, D.J. *TAPPI Coating Conf. Proc.* **1998**, TAPPI Press, Atlanta, pp583-600.

36. Hudspeth, Q.M., Nagle, K.P., Zhao, Y,-P., Karabacak, T., Nguyen, C.V., Meyyappan, M., Wang, G.-C. and Lu, T.-M. *Surface Science,* **2002**, 515 452.

37. Ianoul, A. and Bergeron, A. *Langmuir*, **2006**, 22, 10217.

38. Ishikawa, N. and Satoda, V. *J. Colloid Interface Sci.* **1994**, 162, 350.

39. Israelachvili, J. *Intermolecular and surface forces,* 2nd Ed., Academic Press, San Diego, CA, USA, **1992**.

40. Jacob, P. and Berg, J.C. *Langmuir,* **1994**, 10, 3086.

41. Jeje, A.A. *J. Colloid Interface Sci.* **1979**, 69, 420.

42. Johansson, M. *Licentiate thesis, the Royal Institute of Technology*, Stockholm, Sweden, **2000**.

43. Johnson, R.W. *Tappi J.* **1991**, 74(5): 209.

44. Joos, P., van Remoortere, P and Bracke, M. *J. Colloid Interface Sci*. **1990**, 136, 189.

45. Kan, C.S. and Van Gilder, R.L. *TAPPI Coating Conf. Proc.,* **2004**, TAPPI Press, Atlanta, pp. 21-36.

46. Kistler, S.F. *Hydrodynamics of wetting. In: Wettability,* Berg, J.C. (Ed.), Marcel Dekker, New York, **1993**, pp. 311-429

47. Kubelka, P. and Munk, F. *Z. Tech. Phys.* **1931**, 12, 593.

48. Kubelka, P. *J. Opt. Soc. Am.* 38(5), **1948**, 448.

49. Kubelka, P. *J. Opt. Soc. Am.* **1954**, 44(4), 330.

50. Lavi, B., Marmur, A. and Bachmann J. Langmuir, **2008,** 24, 1918-1923.

51. Leach, R.H. and Pierce R.J. *Printing Ink Manual*, 5th Ed. Blueprint, London, **1993**.

52. Levine, S, Reed, P, Watson, E.J. and Neale G. *"A theory of the rate of rise of a liquid in a capillary" In Colloid and interface science Interface,* Ed. By Kerker, M. Academic, New York, Vol. III, **1976**, 403-419.

53. Lewis, A., Isaacson M., Harootunian, A. and Muray, A. *Ultramicroscopy,* **1984**, 13, 227.

54. LePoutre, P. *Prog. Org. Coatings,* **1989,** 17, 89.

55. Lekelä, M. *"Optical properties", In: Paper physics,* Ed. Niskanen, K., Fapet Oy, Helsinki, Finland, **2000**.

56. Lieberman, K., Ben-Ami, N. and Lewis, A. *Rev. Sci. Instrum.* **1996**, 67, 3567.

57. Ma, D., Carter, R.D., Chen, C. and Hardy, R.H. *TAPPI Coating Conf. Proc*. **2005**, TAPPI Press, CD, Session 27.

58. Ma, D., Carter, R. D., Laine, J. and Stenius, P. *Nord. Pulp Paper Res. J.* **2007**, 22(4), 523-527.

59. Ma, D., Carter, R. D., Laine, J. and Stenius, P. *Nord. Pulp Paper Res. J.* **2008a**, 23(3), 333-337.

60. Ma, D., Carter, R.D, Haefner, D. and Dogariu, A. *Nord. Pulp Paper Res. J.* **2008b** 23(3), 327-331.

61. Ma, D., Carter, R.D, Haefner, D. and Dogariu, A. *Nord. Pulp Paper Res. J.* **2008c,** 23(4), 438-443.

62. Ma, D., Carter, R.D and Bousfield, D. W. *10th TAPPI Coating Fundamental Symp,* **2008**, TAPPI Press, Atlanta, pp121-132.

63. Ma, D., Carter, R. D., Laine, J. and Stenius, P. *Nord. Pulp Paper Res. J.* **2009**, 24(2), to be published in June 2009.

64. Maheu, B., Letoulouzan, J. N. and Gouesesbet, G. *Appl. Opt.* **1984**, 26, 3353.

65. McComb, T.L. and Sreickler, R.H. *"Coloration of aqueous pigmented coatings", In: Paper coating additives*, TAPPI press, Atlanta, **1995**.

66. Marmur, A. J. *Modern Approach to Wettability: Theory and Applications,* Plenum Press, New York, **1992**, pp. 327-358.

67. Marmur, A. *Langmuir,* **1996**, 12, 5704.

68. Marmur, A. *Langmuir*, **2004**, 20, 1317.

69. McCoy, J.W. *TAPPI Coating Conf. Proc.* **1998**, TAPPI Press, Atlanta, pp121-132.

70. Modaressi, H. and Garnier, G. *Langmuir,* **2002**, 18, 642.

71. Moore, D.M. and Reynolds, R.C. *X-Ray Diffraction and identification and analysis of Clay Minerals,* Oxford Univ. Press, New York, **1997**.

72. Nieto-Verperinas, M. *Scattering and diffraction in physical optics*, Wiley, New York, **1991**.

73. Olejnik, S., Posner, A.M. and Quirk, J.P. *Clay Miner.* **1970**, 8, 421.

74. Owens, D. K. and Wendt, R. C. *J. Appl. Polym. Sci.* **1969**, 13, 1741.

75. Paesler, M. A. and Moyer P. J. *Near-Field Optics: Theory, Instrumentation, and Applications*, Wiley, New York, **1996**.

76. Preston, J.S., Elton, N.J., Legrix, A., Nutbreem, C. and Husband, J.C. *Tappi J.* **2002**, 1(3), 3.

77. Rissa, K., Lepisto, T., Vaha-Nissi, M., Lahti, J., and Savolainen A. *Nord. Pulp Paper Res. J.*, **2000**, 15(5), 357.

78. Rame, E. and Garoff, S. *J. Colloid Interface Sci.* **1996**, 177, 234.

79. Reichman, J. *Appl. Opt.* **1973**, 12, 1811.

80. Rohringer, P. and Fletcher, I. TAPPI Coating Conf. Proc., **1996**, TAPPI Press, pp239-251.

81. Romagnoli, A. and Bousfield, D. W. *Tappi J.* **1999**, 82(11), 135.

82. Rousu, S., Gane, P. and Eklund, D. *Nord. Pulp Paper Res. J.* **2000**, 15(5), 527.

83. Rousu, S., Gane, P. and Eklund, D. *Tappi J.* **2005**, 4(7), 9.

84. Schuster, A. *Astrophys. J.* **1905**, 21, 1.

85. Tsang, L., Kong, J.A. and Ding, K.H. *Scattering of electromagnetic waves: Numerical simulations,* Wiley- Interscience, New York, **2001**.

86. Rye, R.R., Mann Jr., J.A. and Yost, F.G. *Langmuir,* **1996**, 12(2), 555.

87. Scaife, J.J., Brake, J.M. and Abbott, N.L. *Langmuir,* **2001**, 17, 5448.

88. Schmalenberg, K.E., Thompson, D.M., Buettner, H.M., Uhrich, K.E. and Garfias, L.F. *Langmuir,* **2002**, 18, 8593.

89. Schoelkopf, J., Ridgway, C.J., Gane, P.A.C., Matthews, G.P. and Spielmann, D.C. *J. Colloid Interface Sci.*, **2000**, 227, 119.

90. Schoelkopf, J., Gane, P.A.C., Ridgway, C.J., Spielmann, D.C. and Matthews, G.P. *Tappi J.* **2003a**, 2(6), 9.

91. Schoelkopf, J., Gane, P.A.C., Ridgway, C.J., Spielmann, D.C. and Matthews, G.P. *Tappi J.* **2003b**, 2(7), 19.

92. Senden, T.J., Knackstedt, M.A. and Lyne M.B. *Nord. Pulp Paper Res. J.* **2000**, 15(5), 554.

93. Shanahan,, M.E. *Langmuir,* **2001**, 17, 8229.

94. Stange, M., Dreyer, M.E. and Rath, H.J. *Phys. Fluids,* **2003**, 15(9), 2587.

95. Synge, E. *Philos. Mag.* **1928**, 6, 356.

96. Tsibouklis, J., Dtone, M., Thorpe, A.A., Graham, P., Nevell, T.G. and Ewen, R.J. *Langmuir,* **1999**, 15, 7076.

97. Tunega, D., Haberhauer, C., Gerzabek M.H., and Lischka, H. *Langmuir,* **2002**, 18, 139.

98. Van Gilder, R.L., Lee, D.I., Purfeerst, R. and Allswede, J. *Tappi J.* **1983**, 66(11), 49.

99. Van Gilder, R.L. and Purfeerst, R.D. *Tappi J.* **1994**, 77(5), 190.

100. Van Gilder, R.L. *Tappi J.* **2004**, 3(1), 7.

101. van Oss, C.J., Chaudhury, M.K. and Good, R.J. *Chem. Reviews*, **1988**, 88, 927.

102. van Oss, C.J., Giese, R.F., Li, Z., Murphy, K., Norris, J., Chaudhury, M.K. and Good, R.J. *J. Adhesion Sci. Technol.* **1992**, 6(4), 413.

103. van Oss, C.J. and Giese, R.F. *Clay Clay Miner.* **1995**, 43(4), 474.

104. van Oss, C.J. *Interfacial forces in aqueous media.* 2nd ed. CRC Press, Boca Raton, FL, USA, **2006**.

105. Wada, K. *Am. Miner.* **1961**, 46, 79.

106. Washburn, E.W. *Phys. Rev*. **1921**, Ser. 2. 17(3), 273.

107. Webb, P.A. and Orr, C. *Analytical Methods in Fine Particle Technology,* Micromeritics, Norcross, Georgia, USA**, 1997**.

108. Werner, O., Wågberg, L. and Lindström, T. *Langmuir,* **2005**, (21) 12235.

109. Wu, S. *Polymer interface and adhesion,* Marcel Dekker, New York, USA, **1982**.

110. Wu, W. *Clay Clay Miner*. **2001**, 49(5), 446.

111. Xiang, Y., Bousfield, D.W., Hayes, P.C. and Kettle, J. *J. Pulp and Paper Sci*. **2004**, 30(5), 117.

112. Yuan, Z., Schmidt, J., Heitner, C. and Zou, X. *Tappi J.* **2006**, 5(1): 9.

113. Zhang, Y. and Sundararajan, S. *Langmuir,* **2007**, 23, 8347.

114. Zhao, Y.P., Yang, H.-N., Wang, G.-C. and Lu, T.-M *Appl. Phys. Lett.* **1996**, 68(22), 3063.

115. Zhmud, B.V., Tiberg, F. and Hallstensson, K. *J. Colloid Interface Sci.* **2000**, 228, 263.